**LOHANNA FERREIRA PAIVA**

# EXPERIMENTAL ANALYSIS OF BIOMIMETIC BLADES FOR SMALL WIND TURBINES

UNIVERSIDADE FEDERAL DE UBERLÂNDIA

FACULDADE DE ENGENHARIA MECÂNICA

**2021**

**LOHANNA FERREIRA PAIVA**

Orientador

**Prof. Dr. Odenir de Almeida**

# EXPERIMENTAL ANALYSIS OF BIOMIMETIC BLADES FOR SMALL WIND TURBINES

**Projeto de Conclusão de Curso** apresentado ao Curso de Graduação em Engenharia Aeronáutica da Universidade Federal de Uberlândia, como parte dos requisitos para a obtenção do título de **BACHAREL em ENGENHARIA AERONÁUTICA.**

**UBERLÂNDIA - MG**

**2021**

# EXPERIMENTAL ANALYSIS OF BIOMIMETIC BLADES FOR SMALL WIND TURBINES

Projeto de conclusão de curso **APROVADO** pelo Colegiado do Curso de Graduação em Engenharia Aeronáutica da Faculdade de Engenharia Mecânica da Universidade Federal de Uberlândia.

BANCA EXAMINADORA

_____

Prof. Dr. Odenir de Almeida
Universidade Federal de Uberlândia

_____

Prof. Dr. Aldemir Aparecido Cavallini Junior
Universidade Federal de Uberlândia

_____

Prof. Dr. Gardolinski Venson
Universidade Federal de Uberlândia

**UBERLÂNDIA - MG**

**2021**

*To my grandmother Dionisia.*

# ACKNOWLEDGEMENTS

First, I would like to thank my parents, Perci and Cicero, and my brother, Nicholas, for all the love they have given me throughout my life. I also thank my grandparents, Dyonisia and Deco for believing in my potential, in me, for their support and encouragement to pursue my dreams, Dalila and Osvaldo, for all their support and strength.

Secondly, I would like to thank Karina for all these years for encouraging and supporting me in times of need, making the bad times lighter and the happy ones so much more fun. I also want to thank Amanda Abigail for her company, support and laughs. You guys made graduation one of the best phases of my life.

I thank my friends and professors at the Faculty of Mechanical Engineering, you were very important in my journey.

I also thank my neighbors and biology teachers Helena Maura and Kleber, and their sons, Augusto, Vergílio and Túlio, for all the help they gave me in this project and in life.

I would also like to thank the Brazilian funding provided by FAPEMIG - Fundação de Amparo à Pesquisa do Estado de Minas Gerais.

Finally, I would like to thank my teacher and advisor Odenir for all the help and attention he gave me to make this project a reality. To the technician Reinaldo Tomé Paulino, for his attention and help in finalizing the test models.

To everyone who somehow contributed to this project, my eternal gratitude.

*“All our dreams can come true, if we have the courage to pursue them.”*

*Walt Disney*

Paiva, L. F. **Experimental analysis of biomimetic blades for wind turbines.** 2021. 103p. Graduation Project, Federal University of Uberlândia, Uberlândia, Brazil.

# ABSTRACT

The theme of sustainability is in high demand in current academic and social discussions and is extremely important for human survival. Among the renewable energy sources, the transformation of kinetic energy contained in the wind into mechanical energy through turbines has been one of the most developed technologies in the last decade, as an alternative to conventional sources. Based on studies by the International Energy Agency - IEA (2017), currently wind energy represents less than 4% of global electricity generated, but it is estimated that in 2050 it will be around 12%. In Brazil, according to ANEEL (Agencia Nacional de Energia Elétrica), currently the participation of wind energy accounts for approximately 10.3% of the total energy matrix

Therefore, the development of the wind turbine projects has been growing gradually over the years. The main efforts of the industry in this sector are currently focused on solving technological limitations of current wind turbines, such as aeroelastic effects, noise effects, placement and maintenance costs, among others. Another problem problem being faced is the it is the design of the blades, which are usually made for specific working configuration purposes, which means that the turbines achieve maximum efficiency in a very narrow range of configurations such as the angle of attack and aerodynamic coefficients that are achieved at one speed of specific wind (Schubel, 2012).

Some solutions adopted to overcome this limitation are the introduction of tilt control devices (Schubel, 2012), active trailing edge flaps (Castaignet et al., 2014) or placing turbines in a location with known and stable wind currents. Recently, engineers and researchers have begun to more frequently look at nature in search for organic designs that could help innovate and increase efficiency in engineering projects, such as the lack of versatility of small and medium-sized wind turbines.

This work focuses on the study and analysis of the adoption of biomimetic solutions as a way to optimize the performance of wind turbine blades. As a way to, there is an introduction of the main concepts of wind energy and then, with the focus on small wind systems, the seeds are scanned to design the blades based on the proposed morphology, and finally, two models for three-blade turbines were built, one with a conventional format (reference) and the second using a biomimetic solution. The models were built using a 3D printer and were tested in an open section subsonic wind tunnel at LAEX (Experimental Aerodynamics Laboratory) at the Experimental Aerodynamic Research Center (CPAERO) located at the Federal University of Uberlândia (UFU).

***KEYWORDS:*** *experimental aerodynamics, small wind turbine, wind tunnel, biomimetics, anemochoric seeds.*

Paiva, L. F. **Análise experimental de pás biomiméticas para geradores eólicos.** 2021. 103p. Trabalho de conclusão de curso, Universidade Federal de Uberlândia, Uberlândia, Brasil.

# RESUMO


O tema da sustentabilidade está em alta nas discussões acadêmicas e sociais e é de extrema importância para a sobrevivência humana. Dentre as fontes renováveis de energia, a transformação da energia cinética contida no vento em energia mecânica por meio de turbinas tem sido uma das tecnologias mais desenvolvidas na última década, como alternativa as fontes convencionais. Baseado em estudos de Energia - IEA (2017), atualmente a energia eólica representa menos de 4% da eletricidade global gerada, porém estima-se que em 2050 será em torno de 12%. No Brasil, Segundo a ANEEL, atualmente a participação da energia eólica na matriz energética é de aproximadamente 10.3%.

Diante disso, o desenvolvimento do projeto de aerogeradores vem crescendo gradualmente ao longo dos anos. Os principais esforços da indústria desse setor atualmente estão focados na resolução de limitações tecnológicas dos atuais aerogeradores, como efeitos aeroelásticos, efeitos de ruído, colocação e custos de manutenção, entre outros. Outro problema enfrentado é o projeto das pás que normalmente são feitos para fins específicos configuração de trabalho, o que significa que as turbinas atingem a eficiência máxima em uma faixa muito estreita de configurações como o ângulo de ataque e coeficientes aerodinâmicos que são alcançados em uma velocidade de vento específica (Schubel, 2012).

Algumas soluções adotadas para suprir essa limitação é a introdução de dispositivos de controle de inclinação (Schubel, 2012), flaps ativos de bordo de fuga (Castaignet et al., 2014) ou colocando turbinas em um local com correntes de vento conhecidas e estáveis. Recentemente, engenheiros e pesquisadores estão utilizando cada vez mais a observação da natureza como solução para mais projetos inovadores e eficientes que abordam a falta de versatilidade de turbinas eólicas de pequeno e médio porte.

Este trabalho se debruça sobre o estudo e a análise da adoção de soluções biomiméticas como forma de otimizar o desemepnho de pás de aerogeradores. Primeiramente, faz-se uma introdução dos principais conceitos da energia eólica e, em seguida, com o foco nos sistemas eólicos de pequeno porte, realizam-se o escaneamento de sementes para projetar as pás com base na morfologia proposta, e por fim realiza-se a construção de dois modelos para turbinas de três pás, um com formato convencional (*reference*) e o segundo com uso de uma solução biomimética. O modelo foi construido utilizando uma impressora 3D e foi testado em túnel de vento subsônico de seção aberta no LAEX (Laboratório de Aerodinâmica Experimental) do Centro de Pesquisa Aerodinâmica (CPAERO) localizado na Universidade Federal de

Uberlândia (UFU).

***PALAVRAS-CHAVE:*** *Aerodinâmica experimental, turbina eólica de pequeno porte, túnel de vento, biomimética, sementes anemocoricas.*

# LIST OF FIGURES

# LIST OF TABLES

# Table of Contents

# CHAPTER 1

## 1 INTRODUCTION

The burning of fossil fuels (coal, oil, natural gas) in thermoelectric power stations generate major environmental impacts due to the emission of $CO_2$ and polluting gases, in contrast to what happens with renewable sources such as wind energy. This has been shown, in recent decades, as one of the most viable sources of renewable energy, mainly due to its inexhaustible and non-polluting nature. Thus, the study of wind turbines has gained space in academic discussions and scientific production (Martins, 2008).

With technological advances, wind turbines became able to generate a greater amount of energy, until the first wind farms appeared. As electricity consumption has grown in recent decades in residential and industrial areas, governments around the world have been forced to study new sources of energy supply. It is in this context that renewable energy sources are gaining importance.

Although it looks new, wind energy has been used for over three thousand years. In the past, it was used by means of mills, which served to pump or drain water, grind grain and other activities that depended on mechanical strength. Over time, they started to use the force of the winds not only to generate mechanical force, but also electrical energy.

Wind turbines with power capacities and rotor diameters less than $20kW$ and $5m$, respectively, can be classified as small wind turbines, for which typical uses are power generation in small grids for remote communities (mini class: $20kW$ of power, $5m$ in diameter), individual remote homes (mid-range class: $5kW$ power, $2.5m$ in diameter), remote telecommunication or power generation for equipment on boats (micro class: $1kW$ power, $1.5m$ in diameter) (Clausen, Wood, 1999).

Classic turbines are designed to operate within a narrow zone centered on their ideal working points, which vary with state-of-the-art speed ratios. This aerodynamic limitation leads to uncertain power generation in a natural turbulent wind environment, typically involving significant energy and economic losses. Although there are different blade shapes for these types of turbines, they all follow the same idea of collecting the wind. Examples of both types of Horizontal Axis Wind Turbine (HAWTs) are shown in the following section.

## 1.1 SHORT HISTORICAL REVIEW

It is speculated that the origin of the first wind rotors were in classical Greece, Babylon, early Gaul and Saxon England, however there are no references to wind-powered machines in reliable records of ancient and medieval periods (Bennett and Elton, 1899). Shahan (2014) defines that the use of wind for mechanical and electrical purposes is dated in:

- **1st Century A.D:** Heron of Alexandria creates the wind wheel, a wheel driven by the wind that is used to power a machine. He harnessed the power of the wind to power an organ. The windmill blades were attached to an axle that drove a set of pistons up and down to provide power to the organ. The device is illustrated in the figure below:

**Figure 1.** Heron's Windmill Design.

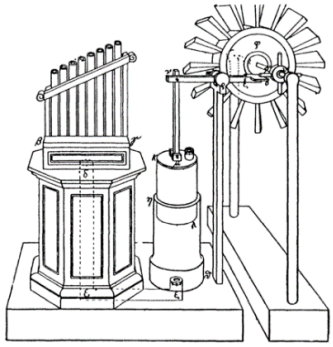

**Source:** Usher (1922).

- **9th Century A.D:** The Persians built vertical axis windmills that were problably used to pump water or grind corn. The vertical sails were most likely made out of reeds and wood. The sails were encased within a set of walls with an open door in front that would guide the wind through the machine as shown in Figure 2.

**Figure 2.** Persian windmill.

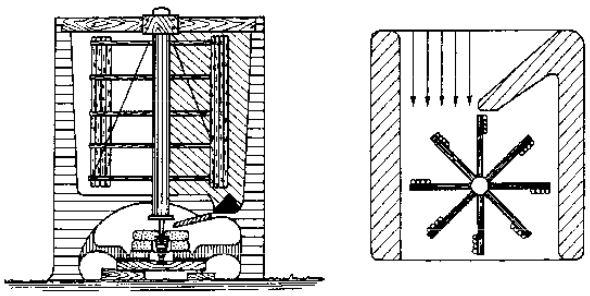

**Source:** Anderson (1979).

- **12th Century A.D:** In the 12th century post windmills were being built in Europe. This type of windmill was built on a vertical post and was set on a rotational post fixture so the entire machine could rotate to face wind (Figure 3). These vertical windmills were usually used for grinding grains or pumping water.

***Figure 3.*** 12th century euroupean post windmills.

**Source:** Anderson, 1979.

- **13th Century A.D:** Tower mills were the newest design in the 13th century in Western Europe. These windmills were built on large stone towers with the rotor and blades attached to a rotating cap that was mounted on top of the tower. A wind vane was also fixed behind the blades to help guide the rotating cap towards the wind.
- **19th Century A.D:** In 1887 American inventor Charles Brush built the first automatically operated wind turbine. It was called a wind turbine, not a windmill, because it was used to generate electricity. The wind turbine weighed four tons and powered a $12kW$ generator.
- Figure ***4*** illustrates what this generator looks like:

**Figure 4.** Charles Brush's wind turbine.

**Source:** Anderson, 1979.

- **1922:** The Savonius wind turbine is a vertical axis turbine invented by Finnish engineer Sigurd Johannes Savonius. The Savonius turbine is a drag turbine meaning that its rotational energy comes from the actual push of the wind, and not from aerodynamic “lift” like most other modern wind turbines.
- **1927:** The Giromill wind turbine is a Darrieus designed vertical axis wind turbine (HAWT). The giromill turbine uses lift instead of drag and is usually built with two or three aerofoils that attach and rotate around a central axis tower as shown in Figure 5. The giromill is a low efficiency turbine because it needs strong wind speeds to start rotating.

**Figure 5.** Components of a Giromill.

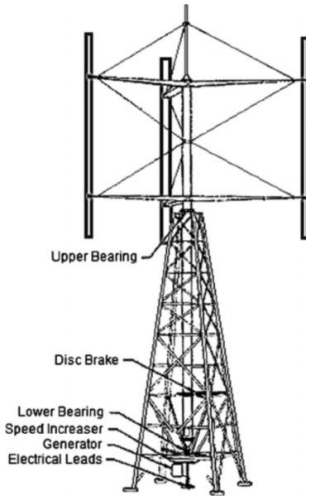

**Source:** Anderson, 1979.

- **1931:** The Darrieus wind turbine also known as the “egg beater” turbine is a VAWT invented by French engineer Georges Jean Marie Darrieus. The egg beater design usually comprises of two or three (Figure 6) aerofoils that rotate around a vertical axis tower with an electrical generator near the bottom of the machine.

**Figure 6.** Original illustrations by G.J.M. Darrieus in 1931 patent: curved blades (a) and straight blades (b). Annotations in thefigure: (a) = blades, (e) = supporting plates, (f1) and (f2) = hubs, (f) and (g) = rotor shaft.

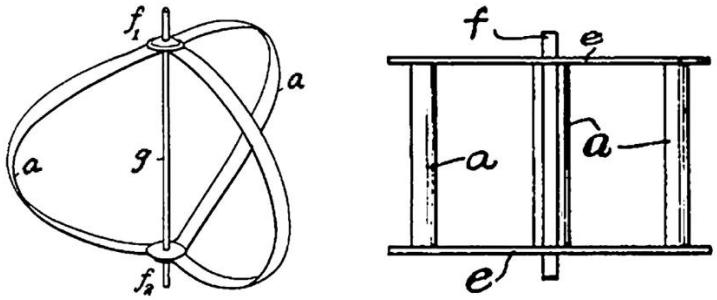


(a) (b)

**Source:** Darrieus, 1931.

- **20th Century A.D:** In 1941 the Smith-Putnam wind turbine became the first megawatt-sized wind turbine to be constructed. It was a two-blade ($175\ ft$ diameter) turbine built on a $120\ ft$ steel lattice tower. It only operated for $1100$ hours until a blade failed.
- **Modern Wind Turbine:** The modern wind turbine was created from years of innovation and scientific research. Today, most modern wind turbines are from the horizontal-axis family and have three blades. The wind turbine blades are designed similarly to airplane wings and use the “lift” from the wind to rotate.

**Figure 7.** Modern wind turbine.

**Source:** Anderson, 1979.

## 1.2 NATIONAL BACKGROUND

In Brazil by 2000, the wind source contributed only to $0.03\%$ of electricity generation in the country (Senado Federal, 2002), jumped to a share of $10.3\%$ in 2021. Although the hydraulic source remains the most important source in our electrical matrix, in 2021 it contributed to the generation of $58.7\%$ (Figure 8) of all electricity in the country.

**Figure 8.** Brazilian energy matrix in GW.

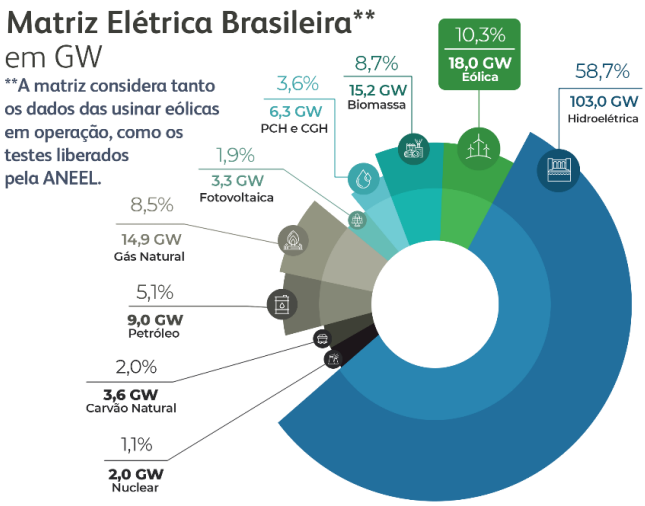


**Source:** ANEEL, 2021.

The first incentive to wind power came with the government program "*Programa Emergencial de Energia Eólica*" (PROEÓLICA) during the 2001 energy crisis, but without producing results. This program had the objective of contracting $1{,}050\ MW$ of wind energy projects by December 2003. At that time, the seasonal complementarity of the wind regime with the hydrological flows in the hydroelectric reservoirs was already known. Subsequently, with the creation of the government program "*Programa de Incentivo às Fontes Alternativas de Energia Elétrica* (PROINFA), in 2002, instituted by Law 10,438/2002, there was a better impact, generating positive results. However, with the end of the projects subsidized by it the current strategy used at the government level is polarized towards the inclusion of this generation through the holding of auctions (Souza, 2018).

The first auction "*Leilão de Energia Reserva* "(LER) that took place in this regard was exclusive to wind energy in December 2009, and was considered a milestone of success. The LER contracted a volume of energy beyond that estimated to meet the country's demand, to be used, according to its name, as a "Garantia Física" (assurance), or backup for the reserve for the electrical system. In this auction, $71$ generation projects were contracted, totaling $1805MW$ (Associação Brasileira de Energia Eólica, 2021). This amount of electrical supply should be available from 2012. Of these, according to the "*Associação Brasileira de Energia Eólica* ", $63$ projects were allocated in the Northeast region, totaling $23$ installations in the state of Rio Grande do Norte ($657$ MW, $21$ in the Ceará ($542\ MW$), $18$ in Bahia ($390\ MW$) and, finally, $1$ in Sergipe ($30\ MW$).

In addition, according to ANEEL (2002), Law No. 10,438/2002 amended article $26$ of Law No. 9427 of December 26, 1996, establishing a 50% reduction in tariffs for the use of electrical transmission systems (TUST) and (TUSD) focusing on the production and consumption of energy associated with wind generation. This subsidy was an additional aid to increase the viability of wind generation in Brazil. Law No. 10,762 of November 11, 2003 limited the benefit of reducing the Tariff for the Use of Electric Transmission Systems (TUST) and Tariff for the Use of Electric Distribution Systems (TUSD) for solar, wind, biomass and qualified cogeneration sources whose installed power were less than or equal to $30\ MW$.

The 2nd LER was a success with the contracting of 1.8GW and opened the doors to new auctions that took place in the following years. In August 2010 the 3rd LER and the Alternative Sources Auction (LFA) were held, where $2GW$ of wind power were contracted. These auctions no longer worked with the exclusively wind model, but instead contemplated several renewable sources competing with each other to trade their energy in the auction. In 2011, three more auction took place, the 4th LER, the A-3 and the A-5, where the wind source had great prominence when negotiating a total of $2.9\ GW$. Finally, in December 2012 the A-5 auction took place, which contracted energy for the beginning of supply in 2017. In this auction, $281.9MW$ were contracted (Multsoluções Energéticas, 2016).

In addition to PROINFA and auctions, the wind source also sells its energy, on a smaller scale, in the Free Market, where contractual conditions are freely negotiated between counterparties. As a result of PROINFA, the auctions held and the free market, at the end of 2012, Brazil has $108$ wind farms totaling $2.5GW$ of installed capacity.

One of the reasons for the growth of wind energy in Brazil is the “good winds”. To produce wind energy, stable winds are needed, with the right intensity and without sudden changes in speed or direction. Brazil is one of the countries that has this type of wind, which has enabled the production of wind energy in recent years (ABEÓLICA, 2018).

**Figure 9.** Evolution of installed capacity (MW).

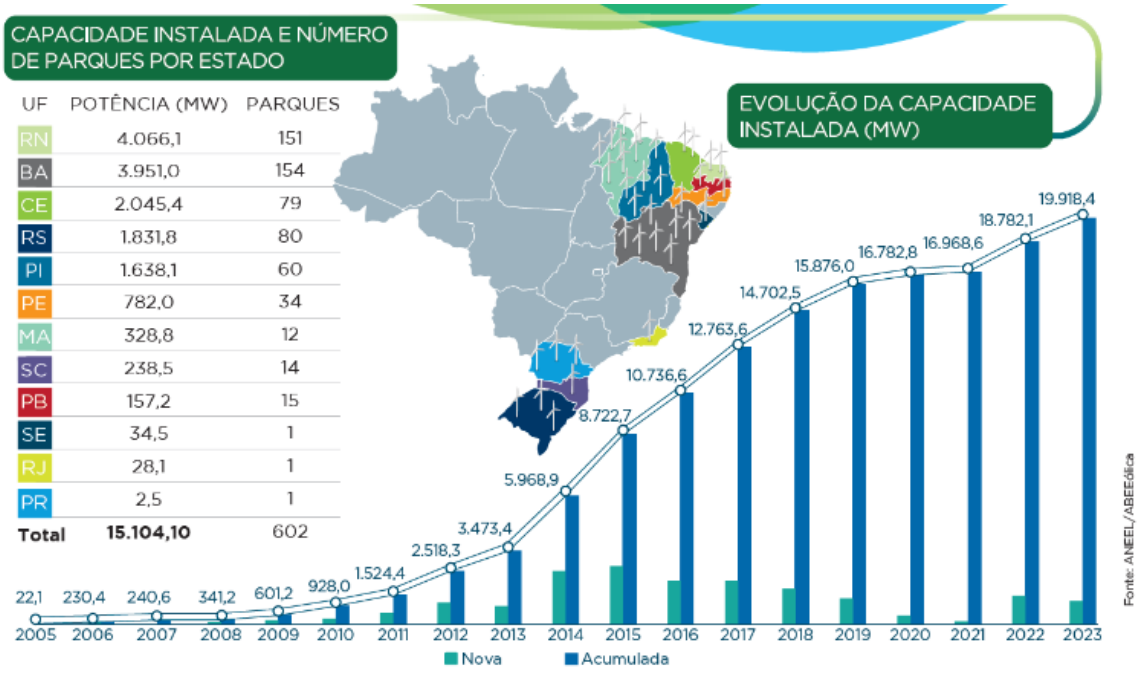


**Source:** ANEEL/ABEÓLICA, 2019.

The good winds in Brazil result in a capacity factor that is almost twice the world average (ABEÓLICA, 2018). While the world average is approximately $25\%$, Brazil has a factor of more than $40\%$, reaching values close to $60\%$ and $70\%$ in the Northeast (MME, 2016). There is a high productivity due to the strength of the winds in Brazil and the growth of active wind farms. Wind energy breaks records in the period of the wind harvest, which is from June to the end of the year (ABEÓLICA, 2018).

Another positive factor for the production of wind energy in Brazil, according to the Brazilian Agency for Industrial Development (ABDI), it is the rapid development of a local and efficient production chain, which began with a nationalization rate close to 60% and reached the manufacture in national territory of 80% of a wind turbine, in accordance with

the financing rules of the Special Agency for Industrial Financing (FINAME) of the National Bank for Economic and Social Development (BNDES) (Mapping the Productive Chain of the Brazilian Wind Industry, 2018, p. 34).

According to data from ABEÓLICA, in 2017, the wind source mitigated the emission of $CO_2$ around $16$ million cars, which is equivalent to twice the vehicle fleet in São Paulo. Landowners have a very significant improvement in their income with the lease to install the towers. Currently, there are more than $6{,}000$ towers installed and operating in Brazil. There is an estimate that more than 4,000 families earn in all, more than $10$ million reais monthly from land leases (Portal energias renováveis, 2019; ABEÓLICA, 2018).

It can also be mentioned that one of the advantages for communities where there are installed wind farms is the possibility of carrying out other activities, such as plantations or animal husbandry, which through the production of jobs, payment flows from leases to landowners, the production of wind energy can influence the fixation of people in the countryside and the training of the local workforce. The wind source has a large positive impact on communities, through social, cultural, health and environmental projects, such as triggering water security programs, making access to water for viable production and human consumption, allowing more isolated populations to have access. In addition, there is a considerable decrease in foreign energy dependence, consequently, dependence on fossil fuels. It is due to all these factors that it can be said that wind energy has a great positive impact on society and the environment (Portal energias renováveis, 2019; ABEÓLICA, 2018).

## 1.3 SMALL WIND TURBINES

Small Wind Turbines (SWT), which range from scaled-down models of their multi-megawatt counterparts to totally innovative design creations, aim at harnessing wind power in urban, near urban or built environment, as well as in populated areas where the implementation of large turbines would not be possible or desirable.

The classification of wind turbines in relation to their size can be done based on the rotor diameter. The figure below illustrates in a simplified way the typical SWT applications and their dimensions, indicating the annual energy generated is a function of the installed capacity, which increases with the increase of the tower height and rotor diameter (Porté-Agel; Bstankhah; Shamsoddin, 2019).

**Figure 10.** Scale of turbines and typical applications.

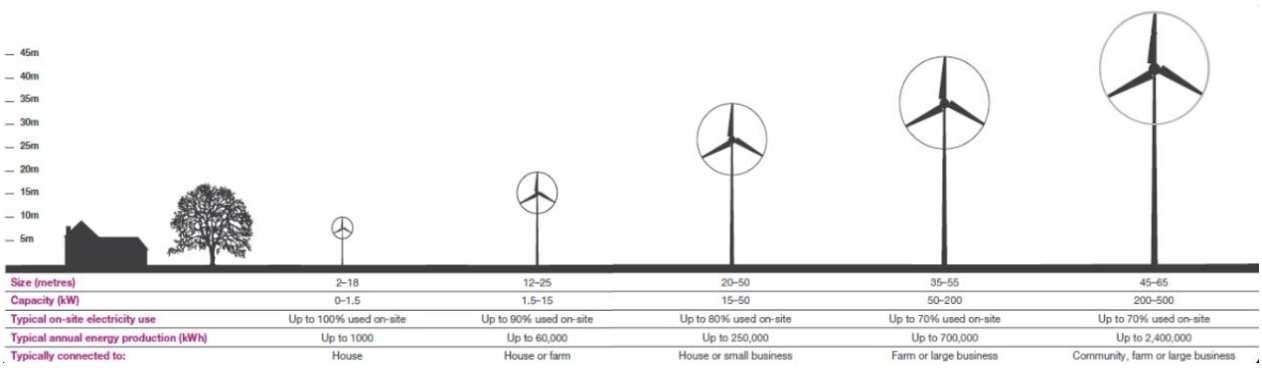


**Source:** Adapted from RenewableUK, 2014.

In addition,

Table ***1*** shows the standard rating system for wind turbines and the effect of the diameter on the rated power of wind generation (Pratical Action, 2012). The diameter of the swept area is twice the length of the blade, which represents the radius of the swept area.

**Table 1.** Standard classification system for wind turbines.

| Scale | Rotor Diameter (m) | | Swept Area ($m^2$) | | Standard power rating (Kw) | |
|---|---|---|---|---|---|---|
| **Smalle scale** Micro | 0.5 | 1.25 | 0.2 | 1.2 | 0.004 | 0.25 |
| Mini | 1.25 | 3 | 1.2 | 7.1 | 0.25 | 1.4 |
| Household | 3 | 10 | 7 | 79 | 1.4 | 16 |
| Small commercial | 10 | 20 | 79 | 314 | 25 | 100 |
| Medium commercial | 20 | 50 | 314 | 1963 | 100 | 1000 |
| Large commercial | 30 | 100 | 1963 | 7854 | 1000 | 3000 |

**Source:** Salih; Mohammed; Taha; Alawsaj, 2013.

Even being a small segment, SWT showed an accelerated growth in the field of renewable energy. In contrast to traditional sources, it is less economically attractive. That said, the US adopted measures to encourage the SWT.

The global wind potential has motivated wind turbine projects for different application ranges. In this scenario, Brazil has a timid share of wind energy in its energy matrix, but this situation is gradually changing. However, Brazil occupies a privileged position in the list of countries with the greatest potential for generating wind energy with promising prospects. The growth of wind power in Brazil has been expressive, but if we analyze its potential, we still have a lot to explore. According to studies by the ANEEL, Brazil has a potential of $300\ GW$ of wind generation, which corresponds to $2.2$ times the Brazilian electricity matrix.

Despite the gradual consolidation of the wind market in Brazil, SWT is still in its early stages, when compared to China and the United States, which have approximately

$573.57\ MW$ and $150MW$ of installed capacity in 2018, respectively. As shown in the Table below, it is possible to notice a growth in excess of $50\%$ between 2013-2018:

**Table 2.** Evolution of installed capacity (MW) and cumulative installed capacity of SWT in variouscountries (2013–2018).

| Country | Installed Capacity (MW) | | | | | | | |
|---|---|---|---|---|---|---|---|---|
| | Cumulative Years before 2012 | By Year | | | | | | Cumulative Years before 2018 |
| | | 2013 | 2014 | 2015 | 2016 | 2017 | 2018 | |
| Brazil | 0.0 | 0.03 | 0.02 | 0.11 | 0.04 | 0.11 | 0.09 | 0.4 |
| China | 280.01 | 75.25 | 69.68 | 48.60 | 45.00 | 27.27 | 30.76 | 573.57 |
| Germany | 24.55 | 0.02 | 0.24 | 0.44 | 2.25 | 2.25 | 1.00 | 30.75 |
| South Korea | 2.99 | 0.01 | 0.06 | 0.09 | 0.79 | 0.08 | 0.06 | 4.08 |
| United Kingdom | 77.98 | 14.71 | 28.53 | 11.64 | 7.73 | 0.39 | 0.42 | 141.40 |
| United States | 130.73 | 5.60 | 3.70 | 4.30 | 2.43 | 1.74 | 150 | 150.00 |
| Other countries | 626.80 | 8.65 | 17.59 | 16.04 | 63.30 | 80.85 | 13.28 | 826.51 |
| Global | 1143.06 | 101.27 | 119.82 | 81.22 | 121.54 | 112.69 | 47.11 | 1726.71 |
| Cumulative | 1143.06 | 1244.33 | 1364.15 | 1445.37 | 1566.91 | 1679.60 | 1726.71 | 1726.71 |

**SWT manufacturers are mainly located in a few countries, with the US, China, Canada, the United Kingdom (UK) and Germany accounting for 50% of their total production capacity (WWEA, 2013).

**Source:** Adapted from DOE (2017).

## 1.4 RATIONALE AND SCOPE

The present work seeks to apply an experimental methodology so that the survey of speed profiles, dynamic torque and Rotation Per Minute (RPM) of two wind turbines (reference and biomimetics) with horizontal axis in the laboratory can be carried out in a simple way, and at a low cost.

These experiments were conducted with the use of a low-speed subsonic wind tunnel at different Reynolds numbers. The speed profile was traced through the aerodynamic fan motor operating frequencies from 20 Hz to 50 Hz, as well as the dynamic torque and RPM for the blade models. Using these experimental data, it was possible to calculate and establish a comparison between the performance of the blades.

## 1.5 RESEARCH OBJECTIVES

In summary, the specific objectives of this work are:

- Design a rigid biomimetic blade HAWT inspired by the adoption two self-rotating seed geometry.

- Experimenting with horizontal turbines (reference and biomimetics) in an aerodynamic tunnel, subjected to different wind speeds and different loads applied to the axle;

- Measurement of torque applied to the turbine by a torquemeter;

- Survey of the speed profiles, static torque curves and power coefficient of the turbines under study from the variables measured experimentally, in order to contribute to the understanding of the performance of the turbine during its operation.

# CHAPTER 2

## 2 WIND TURBINE THEORY

There are several methods for calculating the performance of steady state wind turbines. The most commonly known method of analysis known was developed by Betz and Glauert between 1922 and (Betz, 1926; Glauert, 1926). This theory allows the calculation of the performance characteristics of an annular section of the rotor of an ideal wind turbine. This chapter covers the actuator disk and Blade Element Momentum (BEM) theories.

### 2.1 ACTUATOR DISC CONCEPT

The actuator disk (Figure 11) represents a simple analytical tool to determine information about the flow, showing that the speeds upstream and downstream of the rotor are different from the speed in the rotor plane, in addition to the possibility of estimating the local power coefficient. It is also worth noting that the actuator disk model is obtained from the application of movement to a control volume that contains the rotor. In it, a model used to perform the analysis of the extraction of kinetic energy present in the air for a wind turbine, regardless of its constructive design, where a disk-shaped rotor is considered, considering an infinite number of blades (Burton, 2001). However, the model has, as a limitation, not being able to establish a relationship between rotor geometry and its performance, and cannot be used to optimize the blade to maximize performance.

**Figure 11.** Streamtube of a horizontal axis wind turbine.

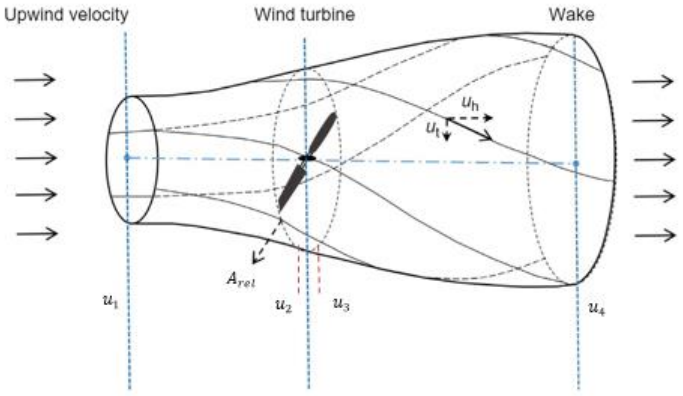


**Source:** Adapted from Neil; Hashemi, 2018.

In developing the model, it is important to highlight the following hypotheses:

- The flow is one-dimensional, incompressible and in a steady state;
- The flow is free (unobstructed) upstream and downstream of the rotor plane;
- The velocity field at the control volume input is uniform, of value $u_0$, static pressure being equal to atmospheric pressure $p_0$.

Figure 11 shows a schematic of a streamtube that is classically used to analyse wind turbines based on actuator disk theory. Because turbine blades partially block and extract energy from the flow, they cause a reduction in the wind velocity at the turbine (or disk), and in the wake of the turbine. Considering the continuity equation in the steady state (i.e.$Q = Au$), this flow reduction means that the flow area will increase at the turbine, and even more at the wake as shown in the figure.

Assuming that there is continuity across the disk, it is possible to define that the speeds in sections 2 and 3 are equivalent to the engine speed:

$$u_2 = u_3 = u_{rel} \tag{1}$$

For steady state flow, air mass flow rate through the disk can be written as:

$$\dot{m} = \rho . A . u_R \tag{2}$$

According to Biadgo and Aynekulu (2017), applying the conservation low of linear momentum to the control volume enclosing the whole system, the net force can be found on the contents of the control volume. That force is equal and opposite to the thrust, $T$ which is the force of the wind on the wind turbine. Hence from the conservation of linear momentum for a one-dimensional, incompressible, time-invariant flow the thrust is equal and opposite to the change in momentum of air stream:

$$T = -\dot{m}(u_{\infty} - u_w) \tag{3}$$

As work is not performed on either side of the turbine rotor, it is possible to use the Bernoulli function in both control volumes on each side of the single actuator. So, between section 1 and 2, free current and downwind side of the rotor, and between section 3 and 4, downwind side of the rotor and the distant mat:

$$p_0 + \frac{1}{2}.\rho.{u_\infty}^2 = p_u + \frac{1}{2}.\rho.{u_R}^2 \quad (4)$$

$$p_d + \frac{1}{2}.\rho.{u_R}^2 = p_0 + \frac{1}{2}.\rho.{u_w}^2 \quad (5)$$

Thrust can also be expressed as the net sum of forces on each side of the actuator disc:

$$T = A.p' \quad (6)$$

where,

$$p' = (p_u + p_d) \quad (7)$$

Using the equations $(4)$ e $(5)$, the pressure decrese, you can find $p'$:

$$p' = \frac{1}{2}.({u_\infty}^2 + {u_w}^2) \quad (8)$$

Replacing equation $(8)$ into equation $(6)$:

$$T = \frac{1}{2}.\rho.A({u_\infty}^2 + {u_w}^2) \quad (9)$$

Equating the equation's buoyancy values$(1.3)$ and substituting the equation $(1.2)$ in place of the equation $(1.9)$ and $\dot{m}$, define the rotor speed as:

$$u_R = \frac{u_\infty - u_w}{2} \quad (10)$$

,

Considering that an axial induction factor is the fractional decrease in wind speed between the rotor plane and free flow, therefore:

$$a = \frac{u_\infty - u_R}{2} \tag{11}$$

$$u_R = u_\infty(1 - a) \tag{12}$$

Using equation $(10)$ and $(12)$ we obtain:

$$u_w = u_\infty(1 - 2a) \tag{13}$$

Biadgo and Aynekulu (2017) define the velocity and pressure distribution are illustrated in Figure 12. Because of continuity, the diameter of the flow field should increase as its velocity decreases and note that there is a sudden pressure drop in the rotor plane, which contributes to the torque of the turbine's rotating blades.

**Figure 12.** Velocity and Pressure distribution along the stream tube.

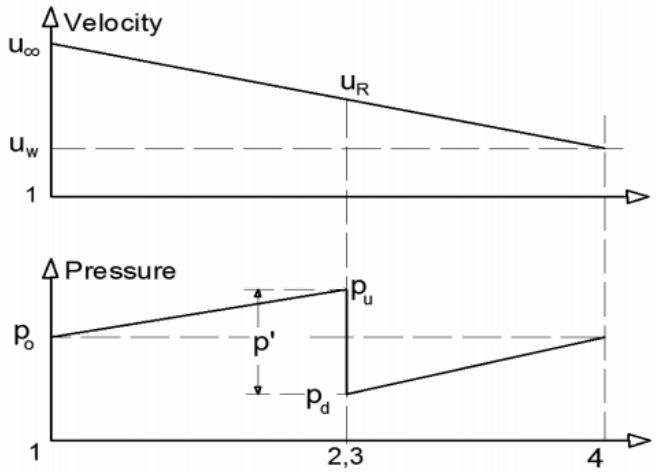


**Source:** Biadgo and Aynekulu, 2017.

The output power can be defined by:

$$P = T.u_R \tag{14}$$

Using the equation $(1.9)$:

$$P = \frac{1}{2}\rho A({u_\infty}^2 + {u_w}^2)u_R \tag{15}$$

or

$$P = \frac{1}{2}\rho A.u^3 \tag{16}$$

Finally, substituting $u_R$ e $u_w$ from equations $(13)$ and $(14)$ on equation $(16)$:

$$P = 2\rho A a(1 - a)^2 {u_\infty}^3 \tag{17}$$

It is possible to express in a dimensionless way the energy performance parameters of a wind turbine, where the energy coefficient, $C_p$, is:

$$C_p = \frac{P}{0.5\rho {u_\infty}^3 A} \tag{18}$$

The average wind velocity at the turbine can be written in terms of the axial flow induction factor $(a)$. An induction factor of 1 means that the wind turbine does not affect the upwind velocity at all ($u_{rel} = u_0$), whereas $a = 0$ means that the turbine completely blocks/stops the wind ($u_{rel} = 0$). Practically, the induction factor is between $0$ and $1$. It can be shown that the power coefficient is a function of the flow induction factor as follows:

$$C_p = \frac{P_e}{P_t} = 4a(1 - a)^2 \tag{19}$$

Similarly to the equation $(20)$, the power coefficient is defined as the ratio between the power drawn from the fluid and the power available in the undisturbed flow field over the disk area. So, the thrust coefficient can be written from Eq. $(9)$ as:

$$C_T = 4a(1-a) \tag{20}$$

Therefore, the power coefficient occurs when the axial factor (a) is equal $a = \frac{1}{3}$, such that:

$$C_{p_{max}} = \frac{16}{27} \cong 0.5926, \qquad C_{T_{max}} = \frac{8}{9} \cong 0.8888 \tag{21}$$

That is, the downstream wind speed must be reduced to one third of the upstream wind speed. Thus, according to the considerations of this model, no motor can extract more than 59.26% of the energy available in the wind in an area corresponding to its diameter, and this limit is the maximum percentage of energy extraction corresponding to the Betz limit (1926).

Figure 13 demonstrates the variation of power and torque coefficients, where the maximum efficiency of an ideal turbine is $59\%$. In the graph, it is possible to observe that the belt speed value is negative and for values less than $0.5$, where empirical methods must be adopted to determine its behavior (Burton et al., 2001). That is, maximum efficiency can only be achieved if the axial induction factor is less than this value. However, in practice, the maximum efficiency of a turbine is lower than the betz limit, due to the effect of factors such as blade drag and tip losses.

**Figure 13.** The variation in $C_p$ and $C_T$ with axial induction factor.

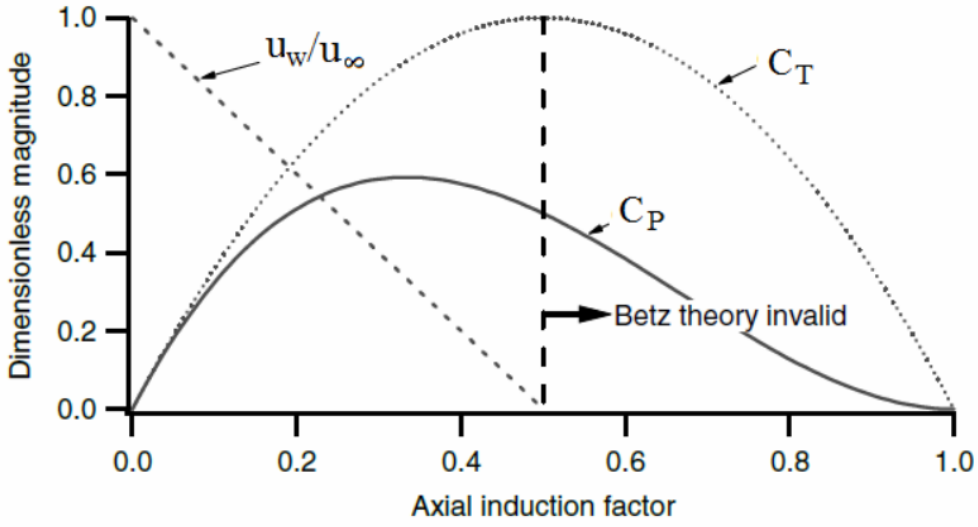


**Source:** Manwell et al., 2009.

Note that the overall turbine efficiency is a function of the rotor power coefficient and the mechanical (including electrical) efficiency of the wind turbine. The actual efficiency,$C_p$, of a wind turbine depends on several variables such as the type of turbine, the geometry, the number of blades and the ratio between the tangential blade tip speed and the wind speed.

**Figure 14.** Comparison of the Betz limit with different types of wind turbines.

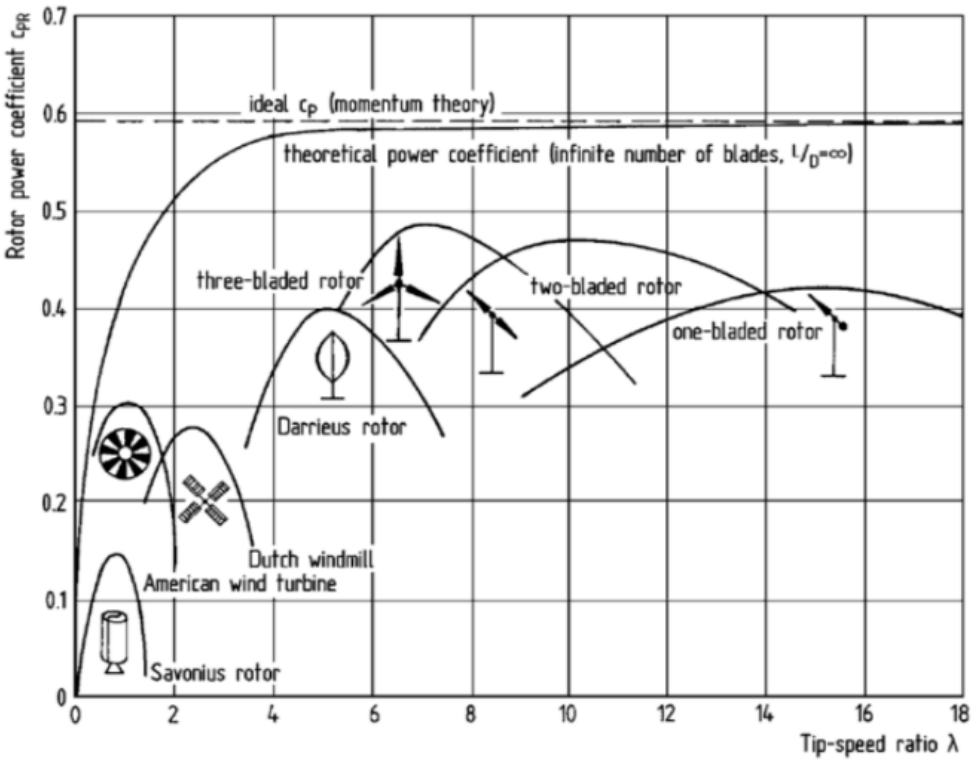


**Source:** Hau, 2005.

Figure 14 represents the approximate value of the different types of wind turbines when compared to the Betz limit, which allows us to have a general reference of the behavior of a turbine according to its type.

The axial thrust on the disk can be written as follows:

$$T = 2\rho A a(1-a)u^2 \tag{22}$$

Conversely, the method presented here yields a solution for the thrust coefficient that is a function of tip-speed ratio while the classical momentum theory predicts that the

thrust is independent of tip-speed ratio. Thus we see that the change in the energy balance caused by the rotational momentum in the slipstream is manifest through a change in thrust coefficient rather than a change in power coefficient for a given axial induction factor. Although the magnitude of the thrust coefficient is less critical in wind turbine design than the power coefficient, the estimate for the thrust coefficient resulting from neglecting the slipstream effects is not conservative. Therefore, designing the tower of a wind turbine to withstand the thrust force predicted by the classical momentum theory could result in structural failure. Similar to the method used to obtain the power coefficient, the thrust coefficient can be described as the ratio of the confidence strength to the dynamic strength, described by the following equation:

$$C_T = \frac{T}{0.5.\rho.u^2.A} \tag{23}$$

An example of the torque versus speed characteristic of awind turbine under steady-state, fixed-pitch and constant windspeed operation is shown in **Figure *15*** for several wind speeds, where the dashed line represents the optimal torque $T$ maximum power extraction.

**Figure 15.** Wind turbine per unit torque versus speed characteristic.

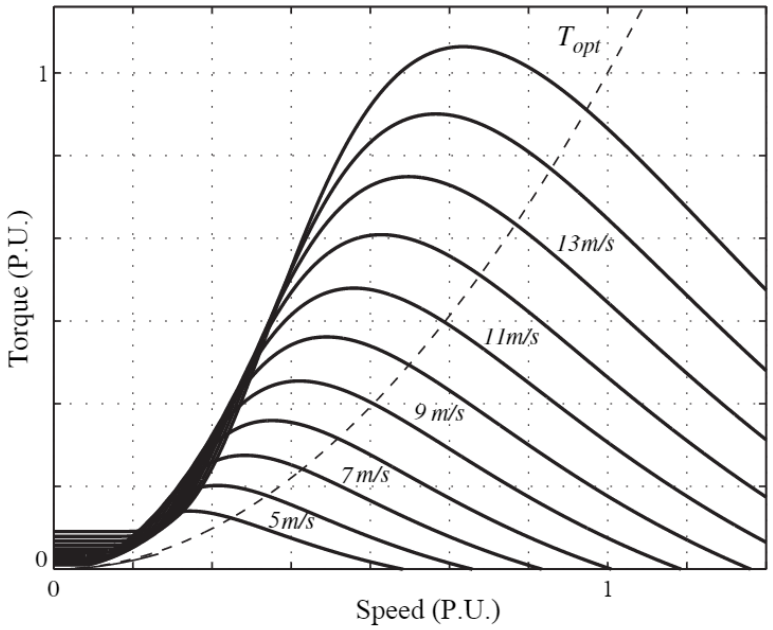


**Source:** Taveiros; Barros; Bezerra Costa, 2013.

## 2.2 THE GENERAL MOMENTUM THEORY

Based on the previous analysis, making use of the linear momentum theory, it can be assumed that no rotation was transmitted to the flow. It is possible to extend this analysis to the case where the rotating rotor generates angular momentum, which may be related to the rotor torque. According to Maxweel et al. (2009), in the case of a rotating wind turbine rotor, the flux behind the rotor rotates in the opposite direction to the rotor, in reaction to the torque exerted by the flux in the rotor. An annular flow tube model of this flow, illustrating disk plane rotation, is shown in Figure 16.

**Figure 16.** Stream tube model of flow behind rotating wind turbine blade.

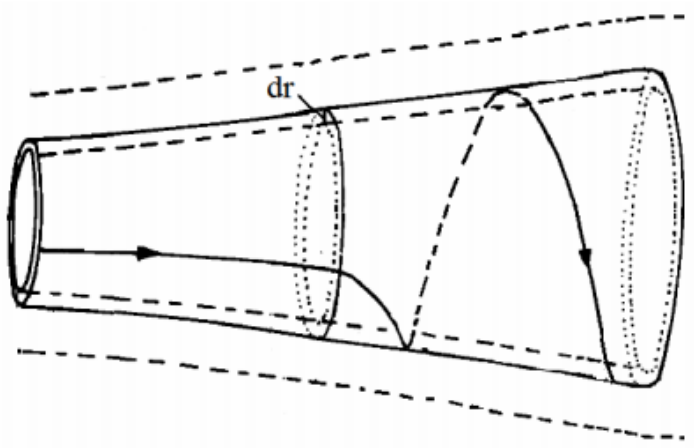


**Source:** Manwell et al., 2009.

The generation of rotational kinetic energy in the wake results in less energy extraction by the rotor than would be expected without wake rotation. In general, the extra kinetic energy in the wind turbine wake will be higher if the generated torque is higher. Thus, as will be shown here, slow-running wind turbines (with a low rotational speed and a high torque) experience morewake rotation losses than high-speed wind machines with low torque.

Assuming the angular velocity transmitted to the flux current,$\omega$, is smaller when faced with angular velocity, $\Omega$, of the wind turbine rotor, then it is possible to assume that the pressure in the distant belt is equal to the pressure in the free flow. Thus, assuming an annular flow tube with radius $r$ and thickness $dr$, a cross-sectional area equal to $2\pi r dr$

Figure ***17***. In addition, belt pressure, induction and rotation factors are all a function of radius.

**Figure 17.** Geometry for rotor analysis.

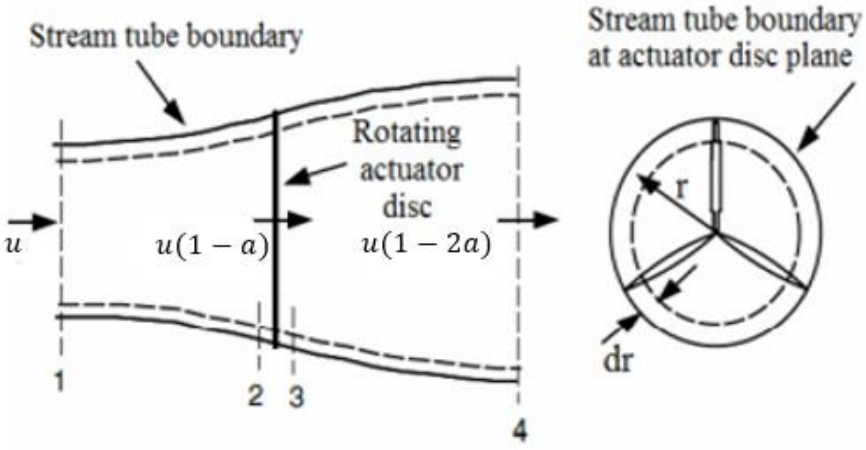


**Source:** Adapted from Manwell et al., 2009.

The wind velocity of the undisturbed air is represented by $u$. $u_1, u_2, u_3,$ and $u_4,$ represent the velocities of air at sections $1, 2, 3$ and $4$ in

Figure ***17***. The wind velocity at the rotor plane, using this simple model, is the average of the upstream and downstream wind speeds:

$$u_2 = \frac{u_1 - u_4}{2} \tag{24}$$

The axial induction factor is, $a$, is defined as

$$a = \frac{u - u_2}{u} \tag{25}$$

The quantity $u_a$ often referred to as the induced velocity at the rotor. The velocity of the wind at the rotor is a combination of the free stream velocity and the induced wind velocity.

$$a' = \frac{\omega}{2\Omega} \tag{26}$$

where $\omega$ is the angular velocity of the flow stream imparted by the wind turbine and $\Omega$ is the angular velocity of the wind turbine. The induced velocity at the rotor consists of not only the axial component, $u_a$, but also a component in the rotor plane, $r\Omega a$'.

The expression for the axial force, $A$, exerted by the fluid on a differential element is given by:

$$dA = 4a(1-a)\rho \mathrm{u}^2 2\pi dr \tag{27}$$

where $\rho$ is the density of the air. The tip speed ratio (TSR), $\lambda$, defined as the ratio of the blade tip speed to the free stream wind speed, is given by:

$$\lambda = \frac{\Omega . R}{u} \tag{28}$$

where $R$ is the tip radius of wind turbine.

The local speed ratio is the ratio of the rotor speed at some intermediate radius,$r$, to the wind speed:

$$\lambda_r = \frac{\Omega . r}{u} \tag{29}$$

The torque, $Q$, on a differential element is given by

$$dQ = 4a'(1-a)\rho u \pi r^3 \Omega dr \tag{30}$$

The result of the general theory of momentum is graphically represented below, which also shows the Betz limit of an ideal turbine based on the linear momentum analysis performed in the previous section. The figure represents the numerical values for, $C_p$, showing that the higher the peak speed ratio, the higher the maximum power coefficient.

**Figure 18.** Theoretical maximum power coefficient as a function of tip speed ratio for an ideal HAWT with and without wake rotation.

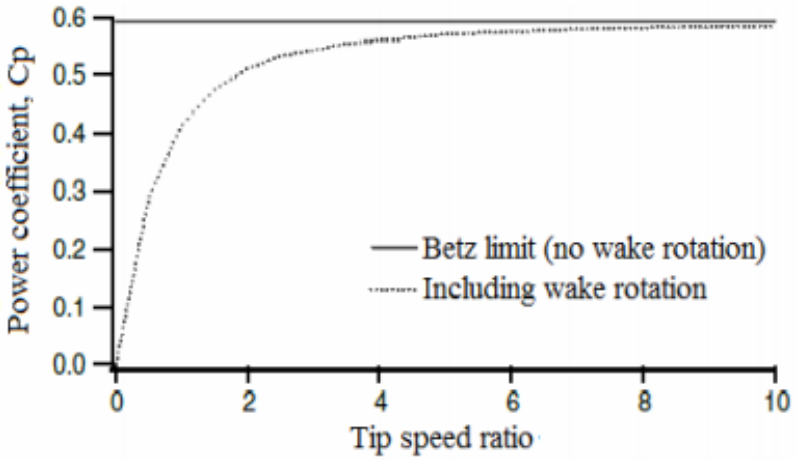


**Source:** Manwell et al., 2009.

## 2.3 BLADE ELEMENT THEORY

The forces on the blades of a wind turbine can also be expressed as a function of lift and drag coefficients and the angle of attack. The blade is supposed to be divided into $N$ sections, called blade elements. Each blade section is independent of each other and aerodynamically operates as a 2D airfoil.

Using the local flow condition, aerodynamic forces are calculated on each airfoil in each blade section. The sum of forces in each section is used to calculate the forces and moments exerted on the blade. It takes some guesswork to explain the Blade Theory Element (BET). It should be considered that there is no aerodynamic interaction between each blade element, not allowing radial flow. Furthermore, it is assumed that the lift and drag characteristics of the blade airfoil shape determine the forces.

Moment theories, developed in the previous sections, are based on a consideration of the mean axial and rotational velocity in the slip current and determine the thrust and torque of a blade from the rate of decrease in fluid momentum. They set an upper limit on the power coefficient of any blade, depending on the free-flowing wind speed and power drawn, but they restrict understanding of the effect of rotor geometry (ie blade airfoil section, chord, and twist). The blade element theory is an alternative method of analyzing the behavior of blades due to their movement through air (Ali, 2014).

**Figure 19.** Theoretical maximum power coefficient as a function of tip speed ratio for an ideal HAWT with and without wake rotation.

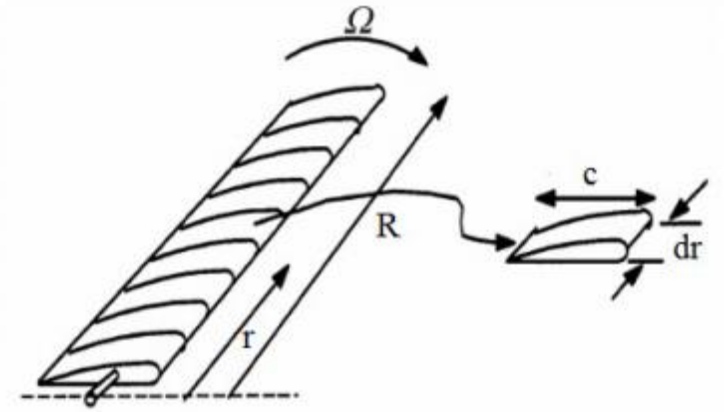


**Source:** Manwell et al., 2009.

**Figure 20.** Blade geometry for analysis of a HAWT.

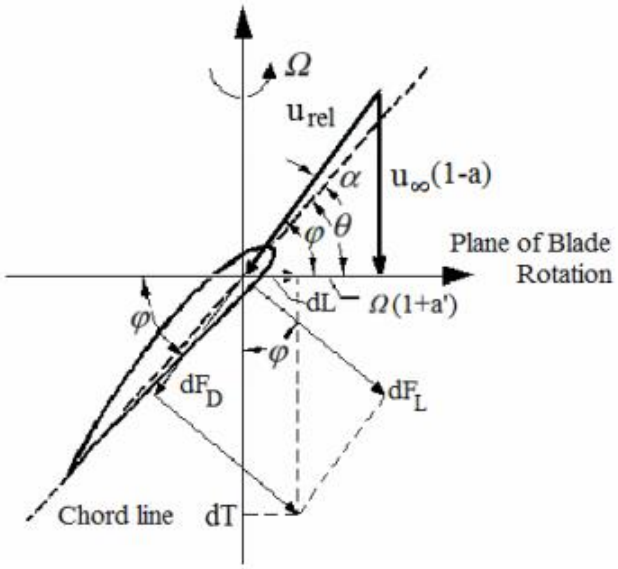


**Source:** Manwell et al., 2009.

A diagram showing the blade element developed in radius $r$ and the velocities and forces acting on this element is given in Figure 20. The relative wind speed urel is the vector sum of the wind speed in the rotor $u(1-a)$ (the vector sum of the free-flowing wind speed, $u$ and the induced axial velocity $-a.u$ and the wind speed due to blade rotation. And this rotational component is the vector sum of the blade section velocity, $\Omega r$,

and the induced angular velocity $a'\Omega r$. Therefore, the relative wind speed will be as shown in the speed diagram in Figure 20. The minus sign in the term $u(1-a)$ is due to the flow delay as the air approaches the rotor and the plus sign in the term $\Omega \mathrm{r}\,(1+\mathrm{a}')$ as shown in Figure 20 it is due to airflow in the reverse direction of blade rotation after the air particles hit the blades and thus give torque.

Here again, only the relevant and most important relations are given for the BE theory. The details can be found in (Manwell et al., 2009).

The induced flow inclination angle is given by:

$$\tan(\varphi) = \frac{u(1-a)}{\Omega \mathrm{r}(1+\mathrm{a}')} \tag{31}$$

The total axial force on the section at a distance, $r$, from the center is:

$$dA = B\frac{1}{2}\rho u_{rel}^2 (C_L.\cos(\varphi) + C_D \sin(\varphi))cdr \tag{32}$$

where, $B$ is the number of blades, $C_L$ is the lift coefficient, $C_D$ is the drag coefficient and $u_{rel}$ is the relative velocity of wind. The differential torque due to the tangential force acting at a distance, $r$, from the center is given by:

$$dQ = B\frac{1}{2}\rho u_{rel}^2 (C_L.\cos(\varphi) - C_D \sin(\varphi))cdr \tag{33}$$

## 2.4 BLADE ELEMENT-MOMENTUM THEORY

BEM theory is a model used to evaluate the performance of a propulsion or extraction turbine based on its mechanical and geometric parameters, as well as on the characteristics of the interaction flow. This model is the result of the combination of the Blade Element Theory and the Momentum Theory, being the first introduced by William Froude, in 1878, to study the behavior of turbines from a local point of view. (Ledoux; Riffo; Salomon, 2020).

In the calculation of induction factors, $a$ and $a'$, accepted practice is to set $C_D$ equal to zero (see Wilson and Lissaman, 1974). So, when the torque equations from momentum and blade element theory are equated (Equations $(30)$ and $(33)$), with $C_D = 0$, one gets

$$\frac{a'}{(1-a)} = \frac{\sigma'.C_L}{4.\lambda_r.\sin(\varphi)} \tag{34}$$

where $\sigma'$ is the local solidity, defined by

$$\sigma' = \frac{Bc}{2\pi r} \tag{35}$$

By equating the axial force equations from momentum and blade element theory (Equations $(27)$ and $(32)$), one obtains

$$\frac{a}{(1-a)} = \frac{\sigma' C_L \cos(\varphi)}{4.\lambda_r.\sin^2(\varphi} \tag{36}$$

After some algebraic manipulations, these equations are solved iteratively to determine the flow conditions and forces at each blade section.

The power contribution from each annular is

$$dP = \Omega dQ \tag{37}$$

The total power from the rotor is:

$$P = \int_{r_h}^{R} \Omega dQ \tag{38}$$

where, $r_h$ is the hub radius.

It is important to emphasize that the BEM theory can only be applied if the blades have uniform circulation, that is, if the circulation is uniform. For non-uniform circulation, there is radial interaction and moment exchange between flows through adjacent elementary annular rings.

### 2.4.1 Power and Torque

This iterative process is started assuming that both induction factors $(a)$ and $(a')$ are zero. The first iterative process results in the determination of $(\varphi)$, $(C_p)$ and $(C_D)$. This process is repeated several times until convergence is reached. Figure 21 shows a typical performance curve for a modern state-of-the-art high-speed wind turbine. The graph illustrates that the maximum power coefficient occurs at a peak speed ratio of about $7$. This corresponds to an axial induction factor that is closer to a value of $1/3$.

**Figure 21.** Performance curve of wind turbine blade.

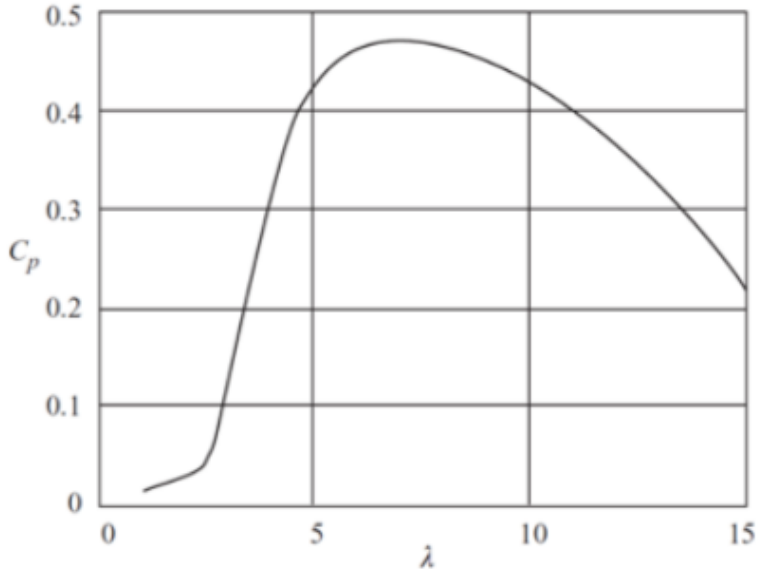


**Source:** Jamieson, 2011.

## 2.5 HAWT BLADE DESIGN

In this chapter, the application of BEM theory in the design of the HAWT blade and the analysis of the aerodynamic performance of a rotor will be explained. The tip loss factor concept, the flow states in which HAWTs are operating, and the introduction of airfoil selection criteria into the HAWT blade design will be discussed. After providing all this necessary knowledge for a blade design, the blade design procedure for an ideal rotor and power performance prediction procedure is provided. It should be noted here that several methods (Zhiquan, et al., 1992; Afjeh, 1989; Goud et al., 1992; Pandey et al., (1989); Nathan, 1980) for HAWT blade design and rotor performance prediction have been studied.

### 2.5.1 The Tip-loss Factor

Due to the pressure difference present in the lower surface and the upper surface of the airfoil, losses occur at the tips. This is due to the tendency of air particles to move from the high pressure region to the lower region. At the tip of the blade, this phenomenon takes effect and usually creates a vortex that dissipates into the conveyor. As a result of this vortex created at the tip, there are losses in the overall energy production of the blade. There are several methods in BEM theory that can be used to measure the losses. The most widely used method is the Prandt method, which introduces a tip loss correction factor.

The tip loss correction factor developed by Ludwig Prandt is:

$$F = \left(\frac{2}{\pi}\right) cos\,. \left[exp\left[\frac{-\left(\frac{N}{2}\right).[1-\ u]}{u}\right]\sqrt{\frac{1+(\lambda u)^2}{(1-a)^2}}\right] \tag{39}$$

The correction factor is a function of angle to wind, number of blades and also blade position. As flow circulation varies from root to tip, the tip loss correction factor allows us to understand the reduction in forces along the blade (Burton; Jenkins; Bossanyi, 2001). Figure 22shows the root-to-tip radial blade tip loss factor.

**Figure 22.** Span variation of the tip loss factor of a wind turbine blade (Manwell et al., 2009).

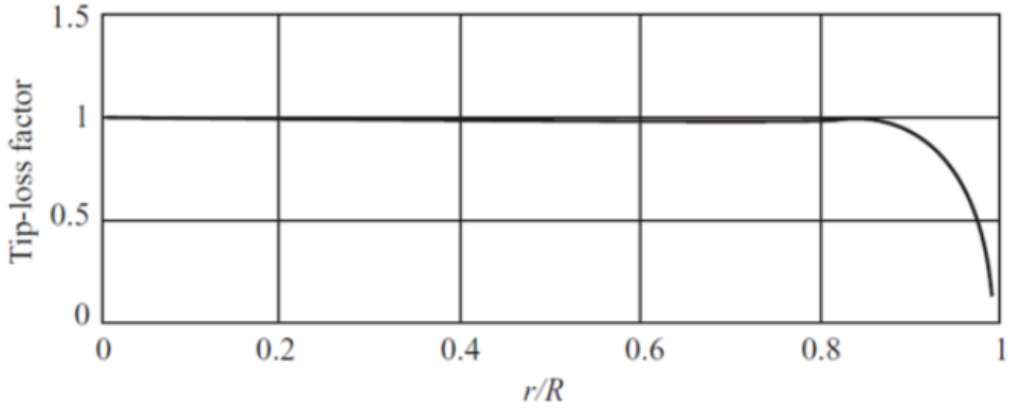


**Source:** Manwell et al., 2009.

The tip loss correction factor ranges from $0$ to $1$. From the blade root to about $85\%$ of the blade radius, a constant factor of $1$ is maintained. However, at the tip, the tip loss factor decreases drastically as you get closer to the tip. This corresponds to the fact that

the induction factor increases dramatically near the tip. As a result, the relative wind speed for a given blade section decreases, as does the angle of attack. This means that the lift and drag forces generated at the tip must also decrease, as they are a function of the relative wind speed and angle of attack (Ali, 2014). This tip loss correction factor characterizes the reduction in the forces at a radius $r$along the blade that is due to the tip loss.

$$dA = F4a(1-a)\rho U^2 \pi r dr \tag{40}$$

or

$$dQ = F4a'(1-a)\rho U \pi r^3 \Omega dr \tag{41}$$

Peak losses are not the only losses suffered by a wind turbine. As with the blade tip, losses at the blade root also occur in a manner similar to that described for the tip. This ends up slightly reducing the thrust and torque contributed by the elements near the tips of the blades.

### 2.5.2 HAWT Flow States

The measured performance of the wind turbine is very close to the results of the BEM theory at low values of the axial induction factors, but the general momentum theory is no longer valid for axial induction factors greater than $0.5$, because according to $u(1-a)$, the wind speed in the distant wake would be negative. In practice, as the axial induction factor increases above $0.5$, the flow patterns through the wind turbine become much more complex than those predicted by general momentum theory. The thrust coefficient represented by Equation $(22)$ can be used to characterize the different flux states of a rotor. Figure 23 shows the flow states and thrust force vectors $T$ associated with a wide range of axial induction factors.

**Figure 23.** Relationship between the axial induction factor, flow state and thrust of a rotor.

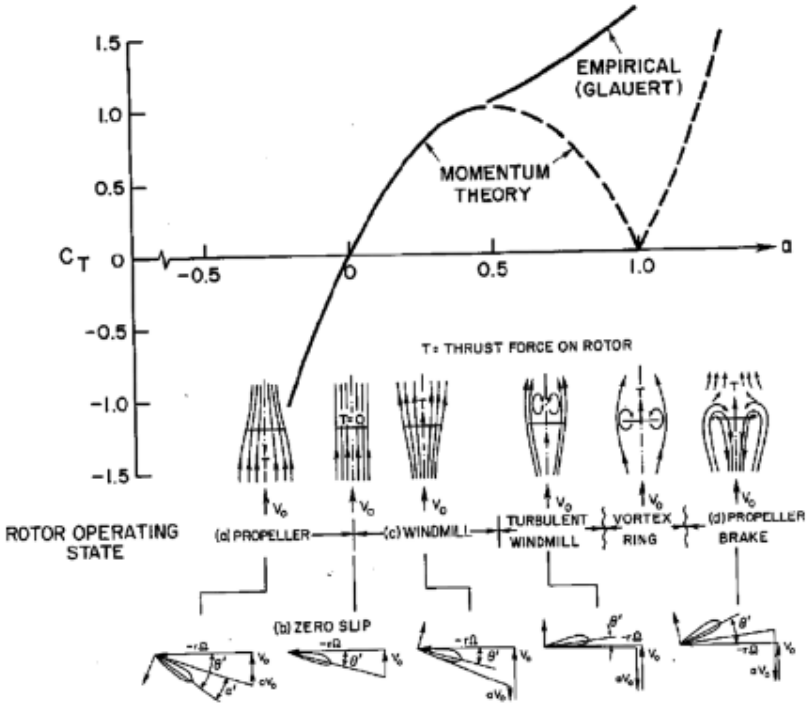


**Source:** Manwell et al., 2009.

According to Figure 23, for negative induction factors ($a < 0$) it is simple to continue the analysis to show that the device will act as a propeller producing a force against the wind (i.e $CT < 0$) that adds energy to the belt. This is typical of the propeller state. The operational states relevant to HAWTs are designated by the windmill state and the turbulent wake state. The windmill state is the normal operating state. The windmill state is characterized by the flow conditions described by the general theory of momentum for axial induction factors less than about 0.5. As illustrated by the data in Figure 23 obtained from wind turbines, above $a = 0.5$, the rotor thrust increases by up to 2 with increasing induction factor in the turbulent wake state, instead of decreasing. While general moment theory does not describe turbine behavior in more detail, Glauert's empirical formula for axial induction factor from $0.4$ to $1.0$ is often used in HAWT rotor design to predict turbine flow states wind (Spera, 1998).

When the induction is just above the unit, the flux regime is called the vortex ring state and when $a > 2.0$ the rotor reverses the direction of flow, which is called the propeller brake state with power being added to the flux to create downwind thrust on the rotor.

In the turbulent waking state, as stated before, a solution can be found using Glauert's empirical relationship between the axial induction factor, a, and the thrust

coefficient, $CT$ in conjunction with the blade element theory (Manwell; McGowan; Rogers, 2002):

$$a = (1/F).\left[0.143 + \sqrt{0.0203 - 0.6427(0.88 - C_T)}\right] \quad (46)$$

This equation is valid for $a > 0.4$ or equivalent for $CT < 0.96$. Glauert's empirical relationship was determined for the overall thrust coefficient for a rotor. It is common, however, to assume that it applies equally to the equivalent local thrust coefficients for each blade section. The local thrust coefficient $C_{T_r}$ can be defined for each annular rotor section as:

$$C_{T_r} = \frac{dT}{\frac{1}{2}.\rho.u_\infty^2.2.\pi.dr} \quad (47)$$

For the elementary buoyancy force of the blade element theory, the local buoyancy coefficient becomes

$$C_{T_r} = \sigma(1-a)^2.\frac{(C_L.\cos(\phi) + C_D.\sin(\phi))}{sin^2\phi} \quad (48)$$

### 2.5.3 Airfoil Selection in HAWT Blade Design

The design of the HAWT blade depends on knowledge of the properties of airfoils. The most significant flow factor that influences the behavior of airfoils is viscosity, which is characterized by the Reynolds number of the airfoil/fluid combination. The Reynolds Re number is defined by:

$$Re = \frac{\rho.u_{rel}.L}{\mu} \quad (49)$$

where, $Re$ is the Reynolds number (dimensioless); $\rho$ is the density of the fluid; μ is the kinematic viscosity of the fluid ($m^2/s$); μ is the dynamic viscosity of the fluid ($kg/m.s$); $L$ is the characteristic linear dimension ($m$).

Furthermore, Mach number compressibility is an important parameter for wind turbine studies and must be considered when combining full scale dynamics. When all these non-dimensional parameters are combined between the stream of interest and the model under test, along with the initial and threshold conditions, the two streams are considered to be dynamically similar. Mach's equation is given by:

$$M = \frac{v}{a} \tag{50}$$

where, M is the Mach number (dimensionless); v is the speed $(m/s)$; a is the speed of sound ($346\ m/s$ at $25°C$);

Airfoils in use in modern wind turbines range in representative rope size from about $0.3m$ on a small scale turbine to over $2m$ on a megawatt scale rotor. Tip speeds typically range from approximately $45$ to $90\ m/s$.

So, for HAWT airfoils, in use in modern wind turbines range in representative diameter size from about $0.3m$ on a small scale turbine to over 2m on a megawatt scale rotor. Tip speeds typically range from approximately $45$ to $90\ m/s$. So for HAWT airfoils, the Reynolds number ranges from about $0.5$ to $10$ million. This implies that turbine airfoils often operate beyond sensitivity. It should be noted that there are significant differences in airfoil behavior at different Reynolds numbers. For this reason, one must be sure that the appropriate Reynolds number data is available for the blade design (Ali, 2018).

There are, of course, many engineering requirements for selecting a wind turbine airfoil. This includes primary requirements related to aerodynamic, structural performance, strength and stiffness, manufacturability and serviceability.

Airfoils for HAWTs are often designed to be used at low angles of attack, where lift coefficients are quite high and drag coefficients are quite low (ie, very low glide ratio). In this thesis, the characteristics of the SG6051 airfoil (Figure 24) were used to create a reference geometry. The SG605X series designed by Selig/Giguere from the University of Illinois at Urbana-Champaign were used because of their good low Reynolds number performance (Selig; McGranaham, 2002). The SG6051 is used from 51% to the tip because of its improved $L/D$ and thinner cross section ($t/c - 12\%$). Additional thickness is added to the root airfoils to further stiffen the blade to account for root bending moment.

***Figure 24.*** *SG6051 (sg6051-il) airfoil.*

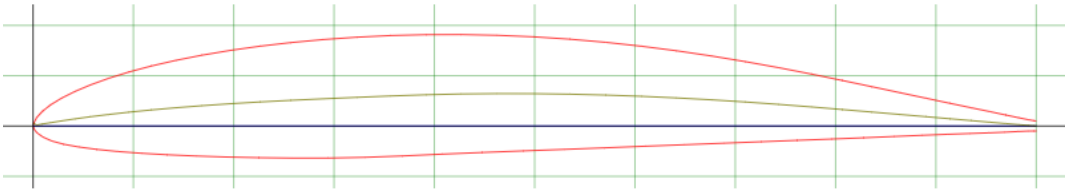

**Source:** AirfoilTools, 2021.

### 2.5.4 Wake Rotation

Linear momentum theory assumes that there is no rotation of flow at the wake of the turbine. However, in reality, the flow out of the turbine is constantly rotating and gradually moves downstream. The torque applied to the turbine by the air moving through it requires an equal and opposite torque imposed on the air. This causes the air to rotate in the opposite direction from the turbine. As the airflow gains momentum, the air particles moving downstream of the turbine consist of a velocity component not only in the axial direction, but also in the tangential direction with respect to the turbine's rotation.

The existence of a rotational flow in the belt results in less energy being extracted by the turbine and as a result kinetic energy losses occur. The most vulnerable wind turbines with large kinetic energy losses that cannot be recovered are those that operate at low rotation speed and high torque (Eggleston & Stoddard, 1987). However, there are minimal losses for wind turbines that have a higher rotational speed and a lower torque.

**Figure 25.** The trajectory of an air particle passing through the rotor disc.

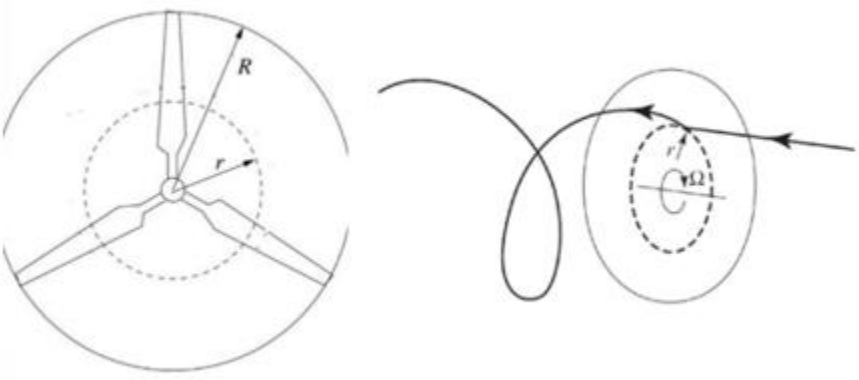


**Source:** Manwell et al., 2009.

As the tangential velocity is not the same for all radial positions, the induced axial velocity varies. For changes to occur in the tangential and axial components of the induced velocity, we must consider an annular ring, as shown in Figure 25, of the rotor disk with radius ($r$) e largura radial ($\delta r$). It is also important to know that the angular velocity of the air relative to the blades increases by $\Omega$ para $\Omega + \omega$. Where $\Omega$ is the angular velocity of the turbine blade and ω is the angular velocity of the air flow in the conveyor.

## 2.6 POWER CURVE

The power of a wind turbine can be characterized through its power curve, that is, the relation between the undisturbed wind speed at the turbine axis height and the output power, as shown Figure 26. Furthermore, the power curve is seen as the main means of evaluating the performance of a turbine.

**Figure 26.** A typical power curve for a wind turbine.

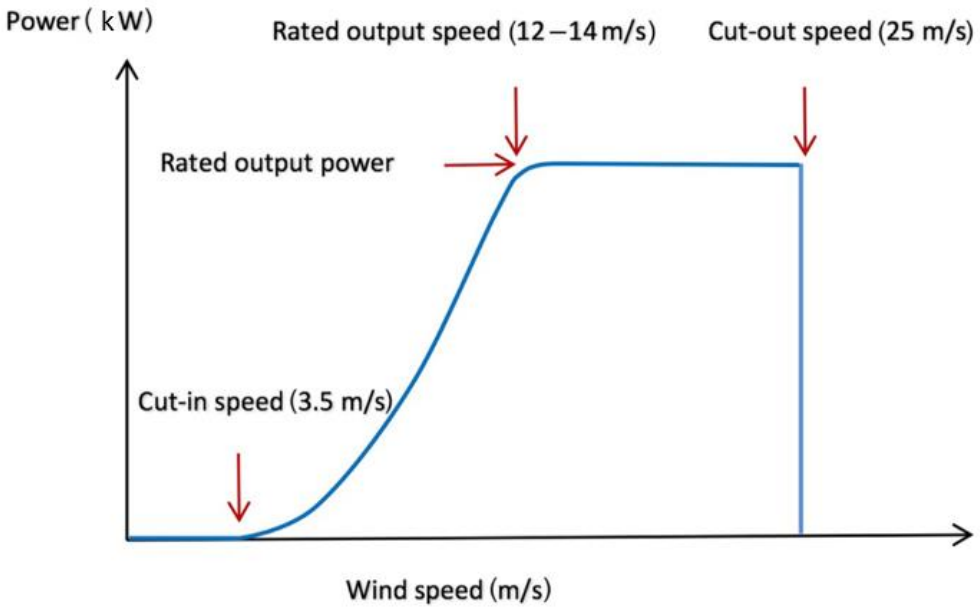


**Source:** Neill; Hashemi, 2018.

Where:

- **Cut-in speed** is the wind speed required for the turbine to start producing power. The wind must reach this speed before the turbine's control system turns the turbine on. This initial velocity is normally found between $3\ m/s$ and $4\ m/s$.

- **Rated output** is the wind speed required for the turbine to reach its maximum power output. So for a 3 MW turbine to reach its full output of 3 MW, the wind speed must reach the rated output speed. As the wind speed rises above the cut-in speed, the electrical energy level increases rapidly. However, typically between $12\ m/s$ to $17\ m/s$, the output power reaches the limit of the capacity of the electric generator. This limit is called the rated power and the wind speed that is reached is called the rated output speed. At higher wind speeds, the design of the turbine is arranged so as to limit the power to that maximum level and there is no further increase in the output power. The way in which this is done varies from project to project, but there are usually controls that keep the power at constant levels.
- **Cut-out speed** is the wind speed that will cause the turbine to shut down and go into a safety mode to protect the turbine from damage. It usually occurs at around $25\ m/s$.

Generally, the power of a wind turbine is given by:

$$P = \frac{1}{2}.\rho.A.u^3.\eta.C_p \tag{51}$$

where, $P$ is the output power, $\rho$ is the air density, $A$ is the engine swept area; $u$ is Nominal wind speed; $\eta$ is the system Efficiency; $C_P$ is the Aerodynamic turbine power coefficient.

# CHAPTER 3

## 3 BIOMIMETICS AS DESIGN INSPIRATION

Since ancient Greece, critics and philosophers have considered living organisms as perfect models with harmonious balances and proportions between the parts of a design, being considered synonymous with the classic ideal of beauty. Architects and designs have drawn inspiration from biology since the beginning of science in the early 19th century. Where we not only sought to imitate the shapes of plants and animals, but also to find design methods analogous to the growth and evolution processes in nature.

Modern research in biomimetics "*Analysis of engineering organisms and their behavior in order to apply the same principles in design*" provides a new name and rigor to what was under the banner of "biotech" in the 1920s and 1930s. The term "Biomimicry" first appeared in the scientific literature was in 1982, and scientist and author Janine Benyus in her 1997 book popularized it, "Biomimicry: Innovation Inspired by Nature". The book brings biomimetics as a "new science that studies models of nature and then imitates or draws inspiration from these projects and processes to solve human problems".

In this way, nature can be considered a model for improving mechanical devices and operations, and as the inspiration for developing entirely new technologies (Benyus, 1997; Vogel, 1998; Forbes, 2005; Bar-Cohen, 2006; Mueller, 2008; Allen, 2010). An important source of innovative ideas came from the fields of biomimicry and bioinspired design. Biomimetics is the field of study that attempts to incorporate new structures and mechanisms inspired by nature into the design and operation of human-based technologies. The biomimetic approach seeks technological advancement through a transfer of innovation from natural systems to engineering systems.

The aim of biomimetics is to produce engineered systems that have characteristics, resemble or function like living systems, particularly in cases where an animal's performance and morphology exceeds current mechanical technology (Vogel, 1998). Exploring nature with the biomimetic or bioinspiration approach attempts to seek common solutions from biology and engineering that allow for greater efficiency and specialization (Vincent, 1990; Ralston and Swain, 2009).

By emulating biological characteristics in cases where the performance of organisms outperforms manufactured devices, the performance of engineered systems can be improved through biomimetics. In addition, engineers can direct the diverse morphological and physiological specializations exhibited in biology to technology transfer and effectively reduce time in developing innovative technology solutions.

Biological organisms are living machines and are subject to the same physical laws as designed systems. These biological machines are fully autonomous, self-powered and self-repairing. The component structures that make up these entities are adapted to particular functions that allow the organism to occupy a specialized environmental functional space, or niche. The multiplicity of biological designs is the result of the evolutionary process of “natural selection” (Darwin1859), in which biological organisms can be considered to have performed “cost-benefit analysis”, optimizing particular designs for specific functions. Biology has therefore provided a design prototype (Allen2010).

In Brazil, biomimetics is still little discussed and studied, with the highlight being the laboratory of the Superior School of Industrial Design (ESDI) of the State University of Rio de Janeiro (UERJ) and the Design department at the Federal University of Rio Grande do Sul (UFRGS). Among the dissertations and theses developed in Brazil, there are: Ramos (1993), Ramos (2001), Salvador (2003), Allgayer (2009), Sette (2010), Detanico (2011), Neto (2013), Rosa (2013) and Reis (2013).

## 3.1 PROBLEM-BASE APPROACH

In 1719, the French entomologist Réne-Antoine Réamur suggested that wasps' use of wood pulp demonstrated an alternative to paper production; this suggestion resulted in the displacement of the production of cotton paper and linen fibers. In 1809, Sir George Cayley studied the aerodynamic shape of dolphins and trout to obtain the ever-lower coefficients of drag hulls (Pawlyn, 2011).

**Figure 27.** Sir George Cayley manuscript illustration.

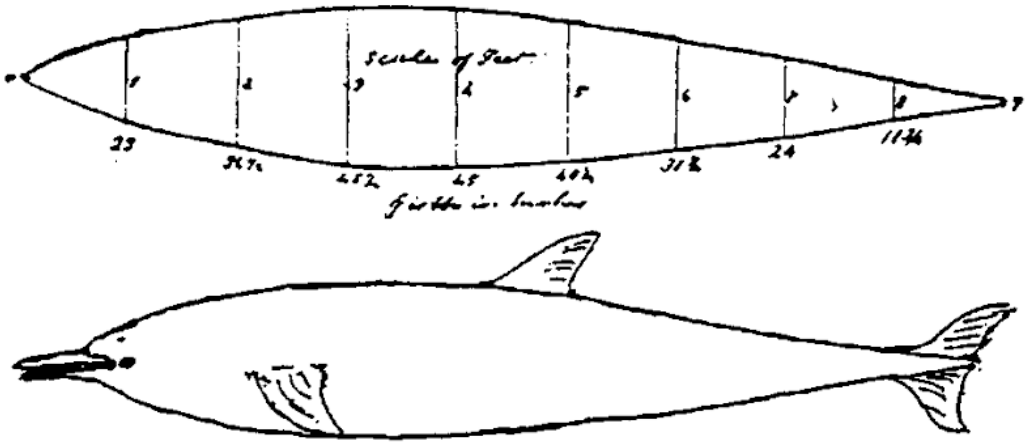

**Source:** Cayley, 1809.

In 2007, Mercedes Company adopted the biomimetic concept for its new boxfish-inspired car (*Ostracion meleagris*), a fish surprisingly aerodynamic due to its box-like shape. Both the chassis and structure of the car are biomimetic, having been designed using a computer modeling method based on how trees are able to grow in order to minimize stress concentrations, as shown Figure 28. The resulting structure looks almost skeletal, as the material is allocated only where it is most needed. (Vincent et al., 2006).

**Figure 28.** Daimle Crysler bionic car inspired by the box fish and tree growth patterns.

**Source:** Zari, 2007.

The car itself, however, is not a new approach to transport. Instead, small improvements were made to existing technology without a re-examination of the idea of the car itself as an answer to personal transportation (Zari, 2007).

Designers are able to research potential biomimetic solutions without in-depth scientific knowledge or even collaboration with a biologist or ecologist if they are able to observe organisms or ecosystems or are able to access available biological research. With limited scientific knowledge, however, translating such biological knowledge into a human design setting has the potential to remain at a superficial level. It is, for example, easy to imitate shapes and certain mechanical aspects of organisms, but difficult to imitate other aspects, such as chemical processes, without scientific collaboration (Zari, 2007).

### 3.1.1 Energy production

Biomimetics has been applied to the design of a number of renewable energy technologies and has provided similar improvements to those we have for building technologies. Marine scientists, in 2004, when investigating the hydrodynamic advantage of whales over other animals, found that it is due to the presence of bumps on the tip of the whale's fin. These bulges cause them to stop more gradually and at a higher angle of attack; therefore, when changing the pressure distribution, make some parts of the flip stall and others don’t (van Nierop, Alben, Brenner, 2008) allows turbines to double their performance and capture more energy at lower wind speeds.

Whalepower, based in Toronto, Ontario, is testing to incorporate the protrusions into commercial products. The wind turbine blade at a wind test facility on Prince Edward Island. The protrusions or “tubers” on the tip, as shown Figure 29, of the blade reduce noise, increase its stability and allow it to capture more energy from the wind. (Fish, 2008).

**Figure 29.** Flippers on humpback whale (left), showing scalloped pattern of tubercles (center) and flipper cross-section (right).

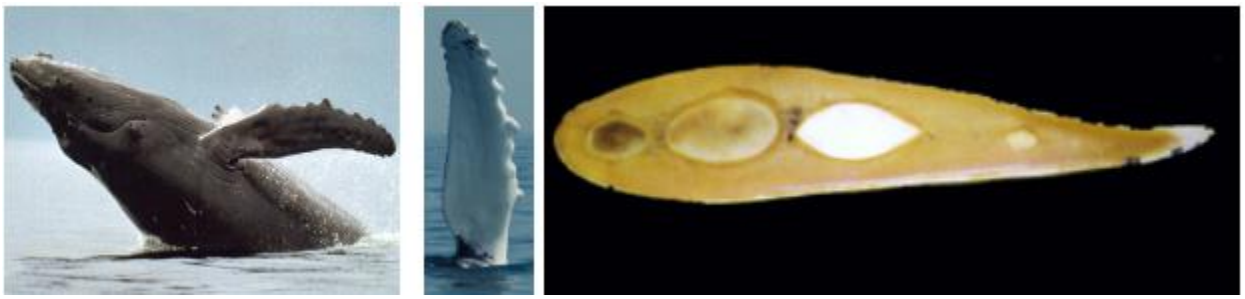

**Source:** Fish, 2008.

The mentioned turbine was able to generate $40\%$ more lift due to the tubers on the leading edges of its blades. Leading edge vortices formed between the protrusions increase the overall angle of attack of the wind turbine.

**Figure 30.** Windmill blade and wind turbine utilizing leading edge tubercles. Courtesy of WhalePower Corporation.

**Source:** Fish, 2008.

Large vortices are formed behind the gutters along the leading edge, while the flow behind the tubercles forms straight lines of flow. The effect of these tubercle-induced flow

patterns is to delay the stall. It is possible to visualize in the figure below the pressure contours and flow lines at $\alpha = 10°$ for NACA 63-021 with straight ends (left) and with tubercles (right). An unstable Reynolds simulation with Navier-Stokes (RANS) mean was used. A separation line is shown in the wing section without tubercles. For the tubercled wing, large vortices are formed posteriorly from the gutters along the outer edge and the posterior flow of tuberculosis is shown as straight flow lines without separation (New, 2020).

**Figure 31.** Pressure contours and streamlines at 10º angle of attack from Unsteady Reynolds-Averaged Navier-Stokes (RANS) simulation, using a total grid size of 400,000 points and based on a NACA 63-021 foil without (left) and with equally spaced tubercles (right) under simulated turbulent flow conditions correspond to Re=1,000,00.

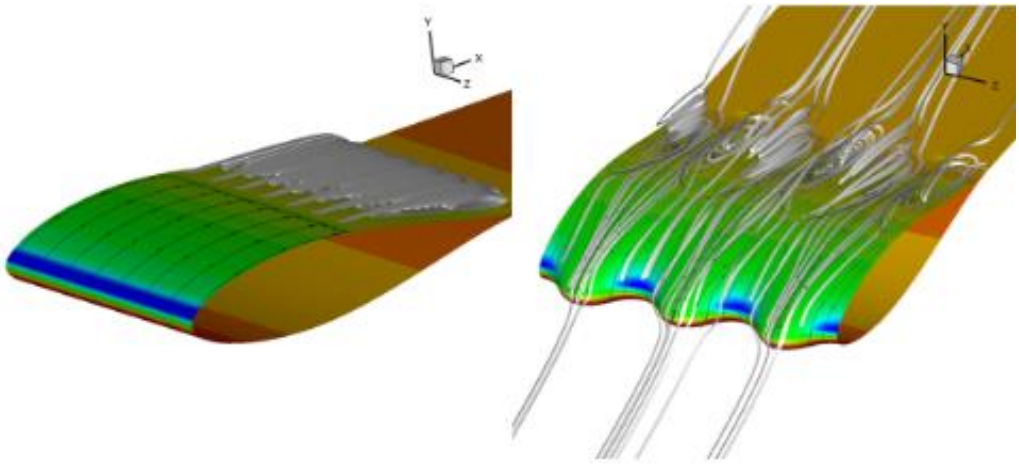

**Source:** Fish, 2008.

Summer, Watters e Masson (2010), studied onboard, for its rotating aerodynamic behavior as they fall, providing good performance characteristics compared to current wind turbines. More recently, Chu and Chong (2017) carried out a study of the performance of rigid biomimetic HAWT rotor blades with different solidity inspired by the seed *Dryobalanops aromatic* (Figure 32), which presents similar behavior to the maple seed, since this seed also rotates during your descent.

**Figure 32.** (a) Side view and (b) bottom view of a *Dryobalanops aromatic* seed sample.

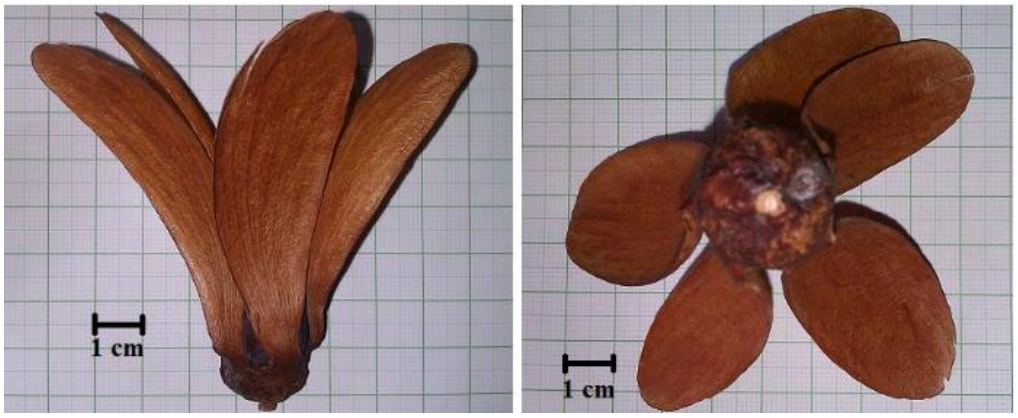


**Source:** Chu; Chong, 2017a.

This study was carried out with the open source computational fluid dynamics (CFD) software *OpenFOAM*®. When compared to a wind turbine with conical blades and torsions by Krogstad and Lund (2012) the starting torque is at TSR $\lambda = 772\%$. It also works in low wind speed conditions due to its ability to generate greater torque during rotation.

**Figure 33.** Upwind (a) original and (b) reduced solidit y biomimetic upwind HAWT.

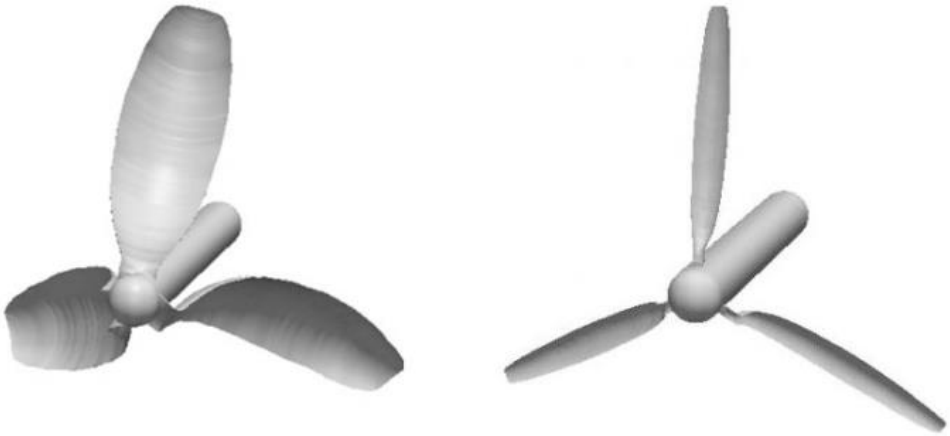

(a) (b)

**Source:** Chu; Chong, 2017a.

Overall, nature-inspired turbines are being investigated to provide better performance and offer a solution to aerodynamic problems. Some of the best known

biomimetic wind turbines are the Maple and *Dropbalanops aromatic* seeds. This behavior makes these seeds suitable to mimic the design of wind turbines, therefore, it is expected that this attribute can be used to efficiently transform wind kinetic energy into mechanical energy. (Gaitan-Aroca; Sierra; Contreras, 2020).

# CHAPTER 4

## 4 MORPHOLOGY DESIGN AND DISPERSAL POTENTIAL OF WIND-DISPERSED DIASPORES OF NEOTROPICAL TREES

Seed dispersal is a key process in the life cycle of plants and understanding this process in natural communities, from an ecological and evolutionary point of view, can help predict the environmental factors necessary for the reproduction and survival of vegetation, aiding conservation and recovery work in areas degraded, such as those present in the Cerrado biome.

This biome is a plant complex that has different phytophysiognomies, grouped into three main formations: forests, savannas and grasslands (Ribeiro, Walter, 2008). In each of these formations prevailing species of flora with different forms of life, reproduction and growth strategies, and the distribution of vegetation is conditioned by several environmental factors. (Eiten 1994; Ratter 1997). Considering the primary type of dispersion, associated with the morphological characteristics of the diaspores, we have:

**Table 3.** Classification of dispersion syndromes.

| Dispersion | Features and Adaptations |
|---|---|
| Zoochory | Dispersion by animals. Fleshy fruits, with food reward for fauna (associated with endozoocoria or synzoocoria), usually with a striking color; nuts with aryl or carunculated seeds, or colored and mimetic aryl seeds; dry fruits with the formation of fleshy pseudofruit or production of aromatic oils and resins; or diaspores without color, odor or nutritional reward, but with structures capable of adhering to the animal's body (associated with epizoocoria) |
| Anemochory | Dispersion by the wind. Fruits or seeds with wings or feathers, capable of floating in the air; or tiny, light seeds that are carried by the wind. |
| Autochory | Dispersion by “the plant itself”. Dried fruits with explosive opening or elastic dehiscence, capable of throwing seeds at certain distances from the mother plant (active autochoria); or diaspores without any evident adaptation to specific dispersing agents, being passively released from the mother plant when mature (passive autochory). |

**Source:** Peres, 2016.

## 4.1 ANEMOCHORY SEEDS GEOMETRY AND ROTATIONAL PROPERTIES

It is possible to classify wind-scattered seeds into two types: pappose seeds (parachute type) and winged seeds, within that there are other sub-classifications (*Table 3*), as illustrated in Figure 34. Pappose seeds used the force of the cloth acting on the pappi (Greene, 1990), while the winged seeds mainly use the lifting force on their wings (Nathan, 2006).

**Figure 34.** Morphologies of the diaspores of 34 tree species using wind dispersal on Barro Colorado Island, Panama.

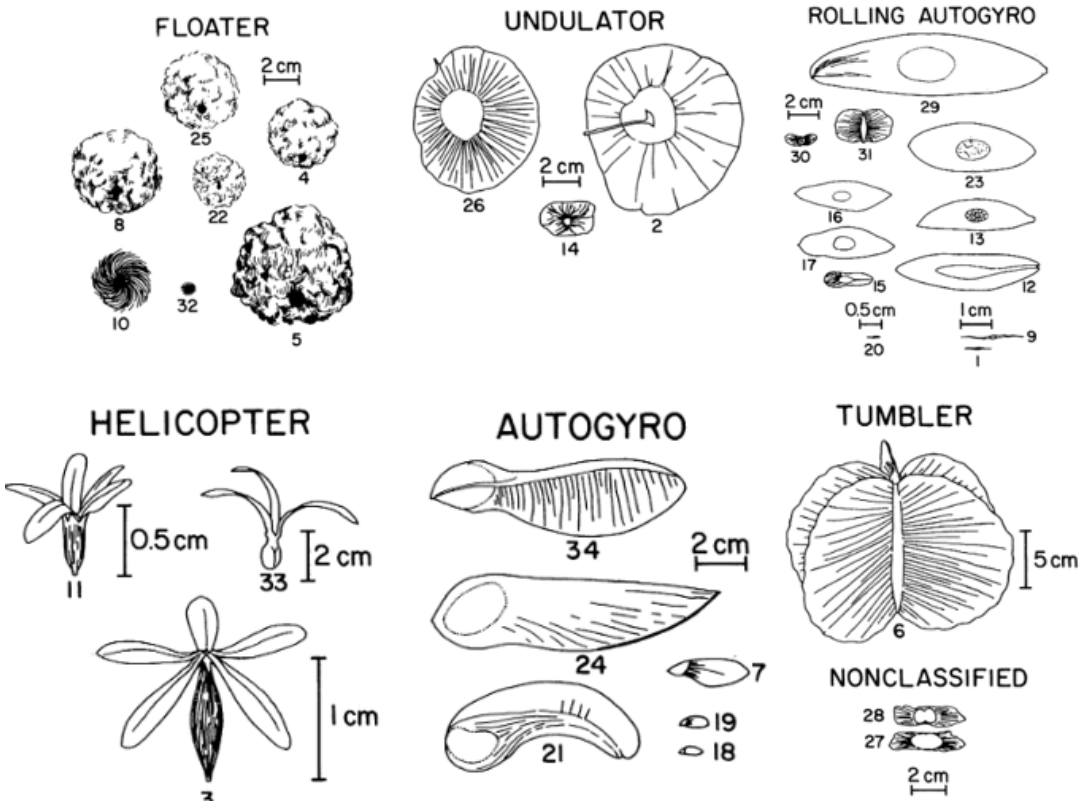


**Source:** Augspurger, 1986.

**Table 4.** A description of the aerodynamic behavior of morphological groups of wind-dispersed diaspores.

| Aerodynamic group | Aerodynamic behavior in still air |
|---|---|
| Floater | Floats downward in a vertical line |
| Rolling autogyro = Flettner-Rotating Autogyro (Vogel, 1981) = "Rolling Samara" (Green, 1980) | Rotates on two axes simultaneously;<br>(1) Around diaspore's longitudinal axis;<br>(2) Around one end of the diaspore in a semi-tight spiral. |
| Autogyro = Lift-producing Airfoil (Vogel 1981) = "Non-rolling Samara" (Green, 1980) | Rotates tightly around the seed end of the diaspore |
| Undulator | Glides and undulates, but not with cumulative forwaed motion (not continuos glider or furgoid oscillator). |
| Helicopter | Spins tightly around a vertical line; similar to autogyro with added wings. |
| Tumblr | Tumbles but not on a consistent axis; radomly |
| Nonclassified | Complex and variable behavior within and between diaspores; closer to autogyro and undulator than rolling autogyro. |

**Source:** Augspurger, 1986.

In the case of autorotation, its movement occurs due to the asymmetric nature of the seeds. The seed's center of mass is well off to one end, while its center of support is roughly in the middle. In a complicated process, the forces at work when the seed falls combine to initiate a circular rotation of the seed around its center of mass, as shown Figure 35. The rotation actually inscribes a cone around the axis of fall. The shape of the cone will vary depending on the aerodynamic qualities of the seed blade (wing). A blade with minimal lifting properties inscribes a steep-sided cone, while a blade with strong lifting properties inscribes a very flat cone (Storm, 2021).

**Figure 35.** Autogyro seed.

**Source:** Adapted from Desenfans, 2019.

The dispersal of winged seeds can be divided into two categories according to the location of their center of gravity. When located in front of the aerodynamic center of the seed, the seed exhibits a glider-like translation during the autumn, without any rotation (Azuma; Okuno, 1987) However, if located near the terminal end of the wing, ie maple and ash seeds, all of them inevitably experience rotation during autumn. It is the main mechanism behind its successful dispersal over long distances, although its wing loading

can be $450\%$ greater than that of sliding and lost seeds, as found by D. Lentink (2009). This high aerodynamic performance can also have wide applications in engineering, particularly in the design of helicopters and new concepts of air vehicles (Siroshi, 2013).

### 4.1.1 Cinematic and Morphology of Autogyro Seeds

According to Lentink et al (2009), self-rotating seeds are able to rotate automatically because their center of gravity, determined by the position of the nut, is located at the base of the wing-shaped seed. Despite their small size and slow speeds, these seeds are capable of generating high lift and can remain in the air longer than other non-rotating seeds. The aerodynamic mechanisms that produce such a lift are, however, unknown.

The function of stable autorotation in maple seeds is to create lift to prolong their descent. This depends on the interaction between the inertial and aerodynamic properties of the seeds, which are not fully understood.

**Figure 36.** Kinematics and morphology of all four autorotating seeds studied. (a) Free-ightparameters: local wing radius, r; local chord length, c; pitch angle, θ; cone angle, β;angular velocity, ω. (b) Free-ight sequence of an autorotating seed showing both the vertical (red) and horizontal, circular translation (blue) of a wing section during afull period. (c) Denition of the local geometric angle of attack and the effective aerodynamic angle of attack, α.

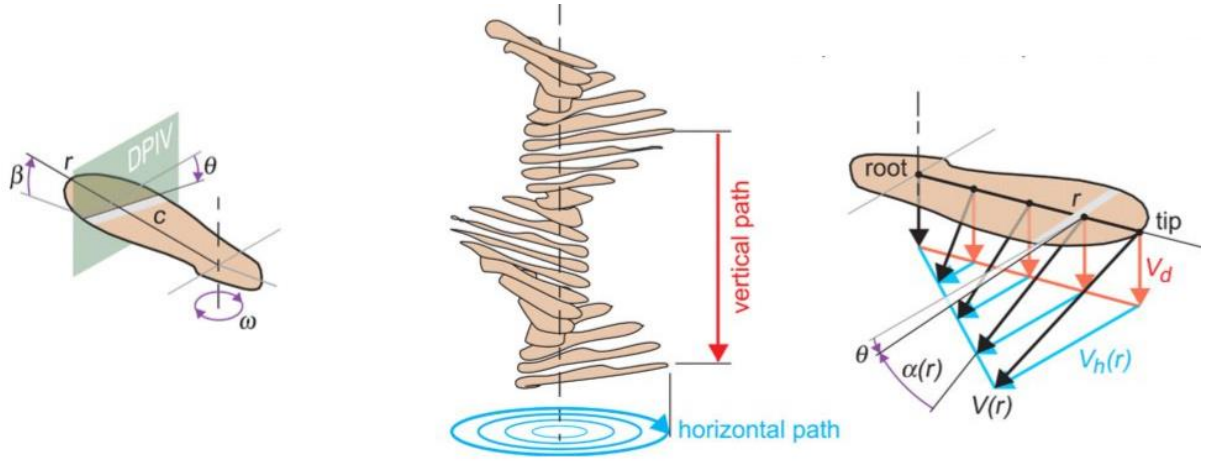


(a) (b) (c)

**Source:** Adapted from Letink et al., 2009.

Letink et al. (2009) demonstrated that seeds generate stable tip vortices that increase lift during descent. Although the wind turbine does not descend, it is believed

that mimicking the geometry of the wing portion of the seeds and converting them into blades will increase the lift generated by the HAWT and thus increase efficiency.

The self-rotating anemochoric seeds have a sophisticated design that allows for robust production of aerodynamic force and stable flight, while showing a high turbulence rejection capability. Seeds protect a wide range of angles of attack as they fall. Furthermore, the morphology design of some seeds is very similar to those predominantly used in wind turbine blades, therefore, the bioinspired design is considered to have the potential to improve the aerodynamic robustness of small wind turbine blades.

## 4.2 *QUALEA MULTIFLORA* & *PEIXOTOA TOMENTOSA*

One of the seeds chosen for this work is *Qualea multiflora* Mart. (Vochysiaceae), also known as pau-terra or pau-terra-do-campo, is a species native to Brazil, widely distributed in the Amazon, Caatinga, Atlantic Forest and Cerrado (Flora do Brasil, 2019) – Figure 37. They have tree habit, twisted branches and are among the most common species in the Cerrado (Ratter et al., 2003), already recommended for the recovery of degraded areas (Bendito et al., 2018).

**Figure 37.** *Qualea multiflora*. (a) flower (b) tree branches showing an open fruit releasing seeds in the wind and a branch with flowers from the previous day.


**Source:** (a) Cunha, K V S (Protographer) 2020, (b) Torezan-Silingardi, H M (Protographer) 2020.

*Qualea multiflora* is an anemochoric species and has a loculicidal capsule-like fruit (Barroso et al., 1999). *Qualea multiflora* is a tree easily found on Cerrado areas.

Another anemochoric species is *Peixotoa tomentosa* A. Juss (Malpighiaceae), a common shrubs from Cerrado vegetation with samarid type fruit (Barroso et al. 1999) – Figure 38. Its floral parts have a yellowish color, characterized by having five petals. This shrub usually has one or two branches that can reach three meters in height, having relatively few leaves, which appear opposite. (Fragola, 1999).

**Figure 38.** *Peixotoa tomentosa*. (a) Flowering branch (b) Samarid type fruit.

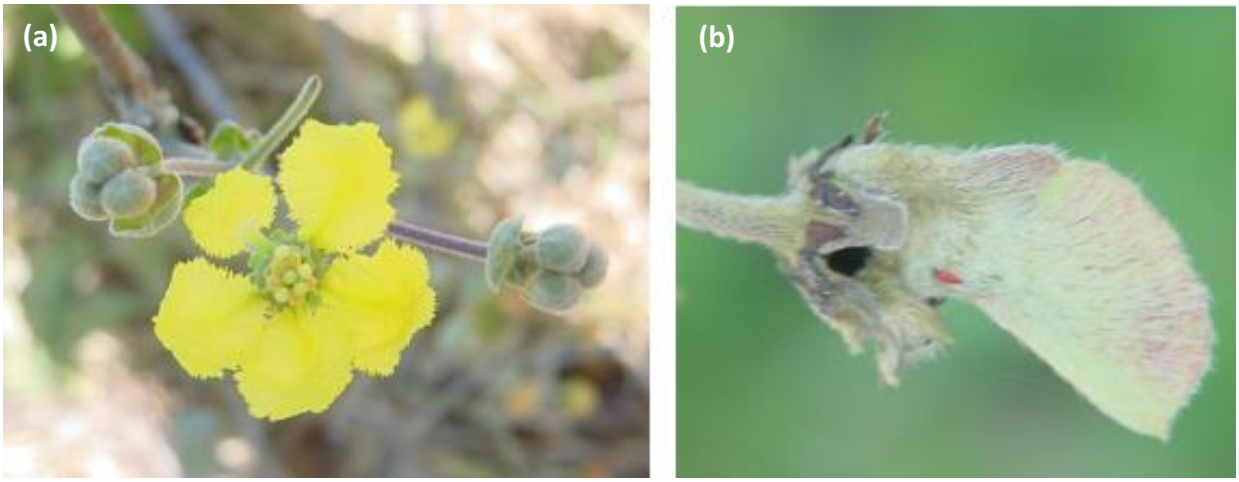


**Source:** Torezan-Silingardi, H M (Protographer) 2020.

# CHAPTER 5

## 5 METHODOLOGY

This chapter is designated for the presentation of the experimental arrangements, the proposed model and the experimental procedure performed on this study.

### 5.1 EXPERIMENTAL SETUP

#### 5.1.1 Collection and Scanning

The seeds used in this work were collected in the private club “Clube Caça e Pesca Itororó de Uberlândia” (CCPIU) reserve (18º59' S and 48º18' W), which is located 8 km from the center of Uberlândia, MG (Figure 39), as part of the research “Environmental variables drive phenological events of anemocoric plants and enhance diaspore dispersal potential: A new wind-based approach” (Novaes et al., 2020), a survey by the Laboratory of Behavioral Ecology and Interactions (LECI) from the Biology Institute (INBIO) in partnership with CPAERO. The reserve covers an area of 127 ha which are protected in the form of Private Natural Heritage Reserve (RPPN). Among the vegetation formations, the cerrado stricto, also with the occurrence of footpaths, forest areas and dirty fields stand out (Appolinário 1995).

**Figure 39.** Cerrado vegetation (red line outline) within the CCPIU.


**Source:** Adapted from Google Earth, 2021).

**Figure 40.** Diaspores of (a) Peixotoa tomenstosa and (b) Qualea Multiflora (Adapted from Novaes, 2020).

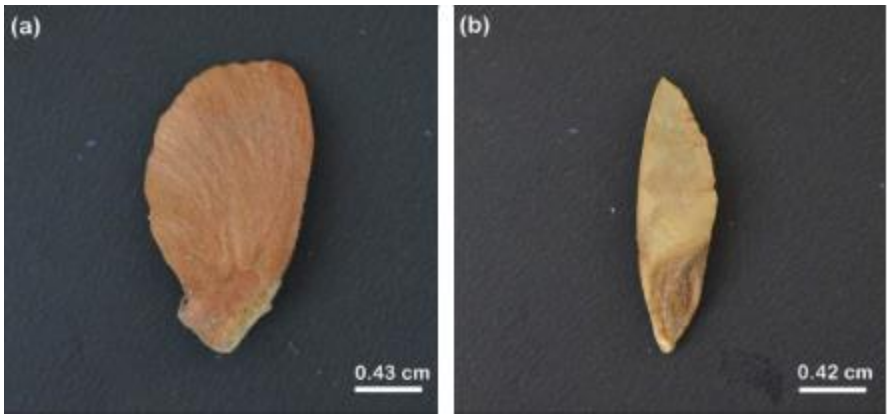


Once the seeds were collected and identified, a 3D structured light scanner was used for computed tomography. They produced high-fidelity, seed-tight parasolide models. The following criteria were established for the 3D modeling that the scan should follow:

- Seed profiling – complete 3D model at scale 1:1 (original).
- Complete 3D model on scale such that the top of the seed has a radius of approximately 250 mm;
- Exclude the protruding region of the seed (embryo protected by a very hard and espresso tegument)
- The scale must be adjusted to reach the $250\ mm$ of the "wing" (wing-shaped) part of the seed.

In possession of this, it was possible to obtain the profile points in the cross sections along the span reproducing the thickness distribution observed in the cross sections of the solid 3D models of the seeds. $25$ and $30$ sections of variable chord length and scaling angle were made to define the geometry of *P. tomentosa* and *Q. multiflora*, respectively.

**Figure 41.** Isometric views of the elements for the biomimetic layer (a) 3D model of the *P. tomentosa* seed; (b) Airfoil sections created from (a) designed to mimic the seed profile; (c) 3D model of the Q. multiflora seed; (d) Airfoil sections created from (c) designed to mimic the seed profile.

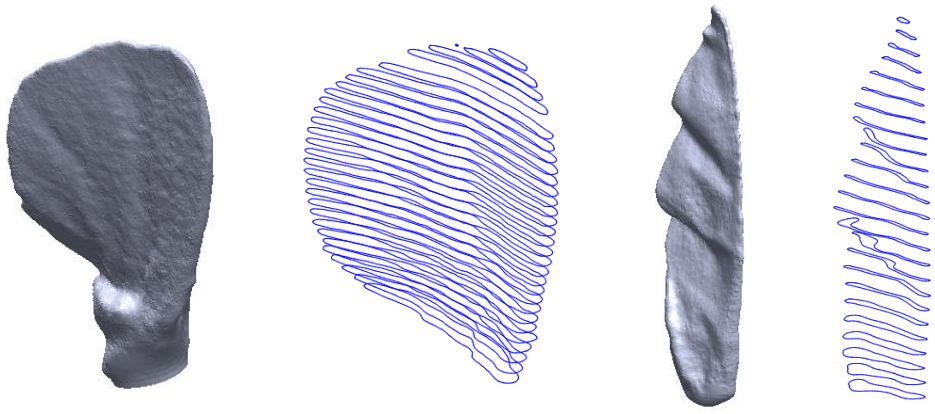

*(a)* *(b)* *(c)* *(d)*

*Figure 41* shows the final 3D sheet after the aerodynamic sections have been imported into *Solidworks*® and a raised surface over the sections. The blade mimics the most interesting geometric features of the maple seed, such as the amplitude scaling variation and trailing edge profile. Figure 42 shows a comparison of the 3D model and a photograph of a seed of the same species. Once the models were created, the analysis process could start with preparing the geometry:

**Figure 42.** The 3D solid part (a) and a photograph of the *Peixotoa tomentosa* seed (b) to compare.

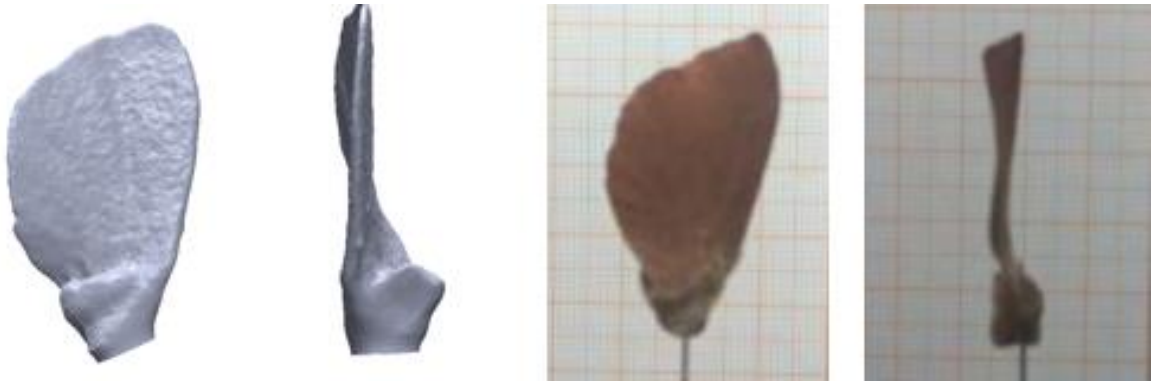

*(a)* *(b)*

### 5.1.2 Model Design

For the study, a conventional upwind HAWT from the study conducted by Ali (2014) was used for validation and performance comparison purposes. This conventional HAWT was called used as a reference in this study (reference). From the airfoils obtained in section 5.1.1, the HAWTs used in this research were modeled. Both biomimetic HAWTs were modeled with their solidity reduced to be the same as the reference HAWT.

As was also shown in the research by Chu (2018), it was noticed that the wings of the seed are leaf-shaped and have an almost constant thickness. Thus, it was proposed that the biomimetic HAWT also has the sheet properties where the thickness of the airfoil is constant. The biomimetic HAWT was sized to follow the size of the reference HAWT, which is $1.2\ m$ in diameter.

The HAWT biomimetic slide was made for a volume amount close to reference. This is done by scaling the biomimetic slides so that they are close in size. The original and reduced solidity biomimetic HAWTs have the same hub diameter, rotor diameter and nacelle length as the reference.

The set of prototype designed for this project is shown in Figure 43. A computer aided design engineering tool, *Solidworks*®, was utilized in designing the prototype. Due to the space restrictions in the test section of the wind tunnel, the height of the system has been kept at $1\ m$ to leave enough space of the wind tunnel. The diameter of wind turbine is approximately $1.335\ m$.

**Figure 43**. Model design of (a) Reference (b) *Peixotoa tomentosa* (c) *Qualea multiflora*.

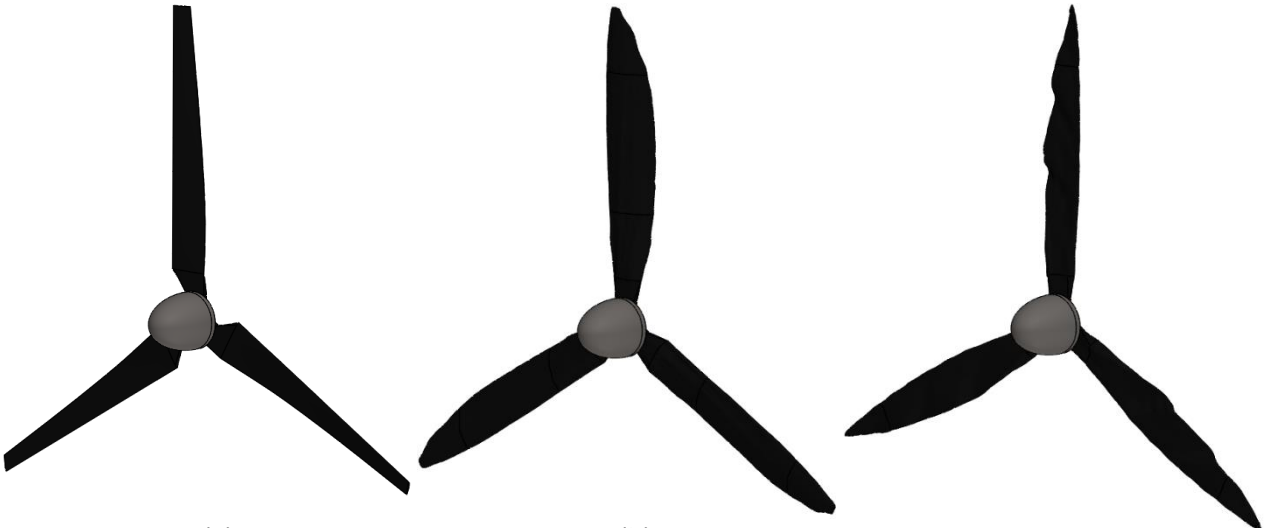

A conventional upwind HAWT from the study conducted by Ali (2014) was adopted for validation and performance comparison purposes. This conventional HAWT was called reference HAWT in this study.

### 5.1.3 Construtive Process

For the construction of the prototype, a 3D printer *Makerbot Replicator Z18®* Figure 44 provided by CPAERO was used.

**Figure 44.** 3D printer Makerbot Replicator Z18.

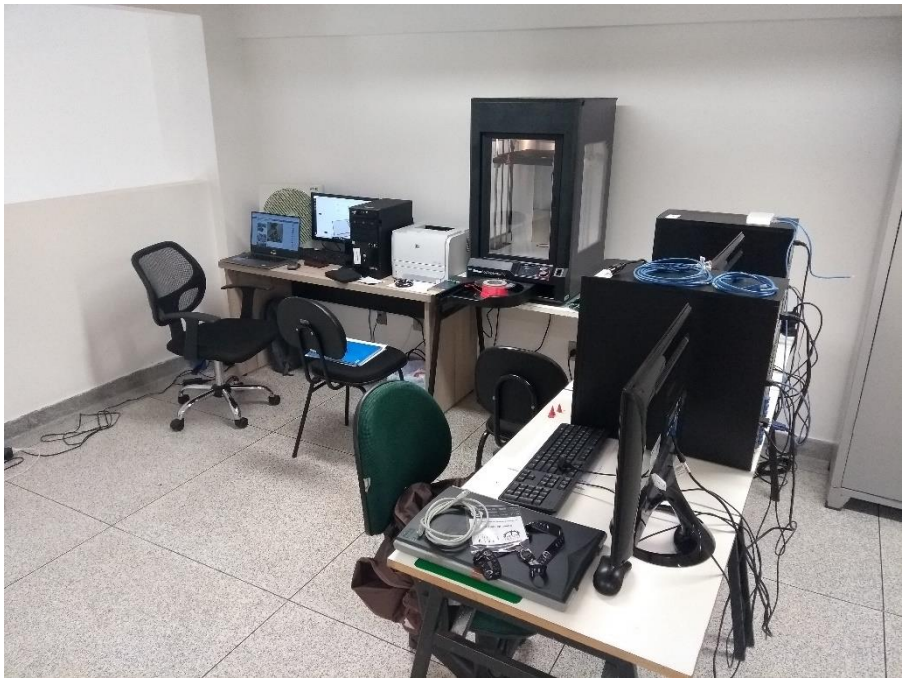

The printer uses 3D printing technology called FDM (Fused Deposition Modeling). Using as printing material the PLA (Lactic Plastic) plastic filament. The process is performed layer by layer, using very fine plastic threads which, through repetition, build the objects (Cliever, 2015). For correct printing, a 3D file must be generated in some CAD software that is recognized by the MarkerBot Print Software (Pro) software, saving it in STL (Standard Triangle Language) format.

As turbine blades are subjected to extremely high bending loads because of the thrust they produce, it becomes very critical for choosing the material selected to have a very high strength property. It is also important to consider the inertia of the blades as it ultimately influences the starting behavior of the wind turbine (Mishnaevsky Jr et al., 2011).

Because of this, the paddles and spinner were manufactured using PLA, a biodegradable thermoplastic derived from cornstarch. Very rigid and resistant, with high hardness, making flexibility difficult. Becoming poorly impact resistant and making it contraindicated for parts, that have snaps (Impressão 3D Fácil, 2015).

Due to the size of the blades, it was necessary to divide them in half and print them separately. For the printing of all blades and the spinner in this study, approximately $80$ hours of printing were required, using two $1\ kg$ rolls each of PLA. Remembering that the top pieces are printed separately as they need to have a different density than the others. With regard to costs, $R\$\ 231.80$ were spent on this process. After being printed, the pieces are joined, sanded and painted. After the treatment with sandpaper, some types of materials are used to reduce the roughness of the blades. The result can be seen below:

**Figure 45.** PLA manufactured wind turbine blades (a) Reference (b) *Q. multiflora* (c) *P. tomentosa*.

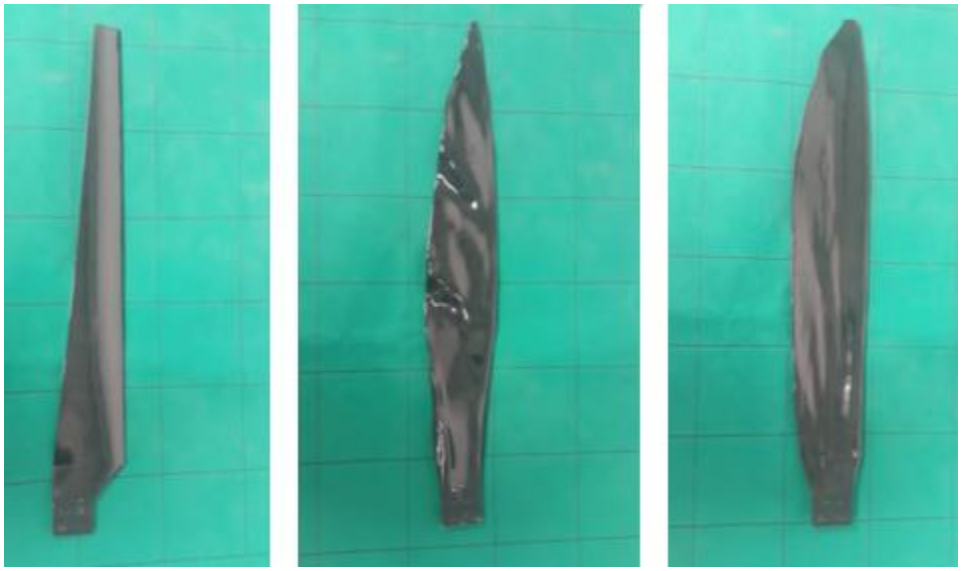

(a) (b) (c)

## 5.2 Experimental Facilities & Instrumentation

### 5.2.1 Wind Tunnel

The facility is an open section subsonic wind tunnel which has a test section of $60\ x\ 60\ x\ 100$ cm. The TV60 wind tunnel is a property of External Aerodynamic Research Center (CPAERO) located in 1DCG building at Federal University of Uberlândia, Glória Campus. Figure 46 and Figure 47 show the wind tunnel and its test section.

**Figure 46.** Wind tunnel TV60 (LAEX/CPAERO, UFU).

The drive system of the wind tunnel comprises a $12$ blade rotor driven by a $25\ HP$ electrical engine responsible for creating the flow momentum in the tunnel. The flow velocity is driven by an electrical inverter which output varies from $0$ to $60\ Hz$, which gives a flow velocity range from $0$ to $28 m/s$. This subsonic wind tunnel is instrumented with pressure taps and analogic manometer. A Pitot tube and a digital manometer are used to calibrate the wind tunnel as well as to collect measured data in some experiments. For this analysis specifically it was used a hot wire anemometer to perform measurements of velocity profile (Silveira, 2017).

One of the limitations of this study at the beginning was due to the loss effect on the blade tips, which could be reduced by increasing the size of the test section. Thus, a diffuser was designed to be coupled to this section, expanding it by $1.69\ m^2$.

**Figure 47.** Wind tunnel TV60 with diffusor.


**Figure 48.** Auxiliary instruments, from left to right respectively, Pitot tube, Kimo and digital thermometer.


This wind tunnel was used to perform an analysis of the flow over a commercial vehicle-pickup in Pinto (2016). In this work, a study of the wind tunnel boundary layer and turbulence intensity was done in order to obtain the wind tunnel characteristics.

### 5.2.2 Pressure module

The pressure distribution, as well velocity calculation using Total pressure probe, can be mapped by the pressure module *AA-TVCR2®* with 64 channels, which allows the

taking of 64 simultaneous pressure taps, allowing, together with its software, to store data according to the user's needs pressure tap the module offers two channels, the so-called high tap and low tap, in which the high tap refers to the pressure to be measured and the low tap the reference pressure.

**Figure 49.** Pressure module AA-TVCR2.

**Source:** Adapted from AeroAlcool, 2021.

A pressure tap consists of a cylindrical tube connected to a hose, connected to the pressure module at the high inlet, the module being connected to a computer, while the reference pressure is connected to another hose, and connected to the low inlet of the pressure module.

### 5.2.3 Measures Methodology

To take the pressures, initially, a device was made where the hoses from the pressure module would be connected to the pressure taps. The pressure module hoses are connected to a rod varying vertically from the center of the wind tunnel to $6\ cm$ before the lower wall of the diffuser and in $6\ cm$ increments thereafter, as can, as can be seen in:

**Figure 50.** Pressure device for velocity profile measurements.

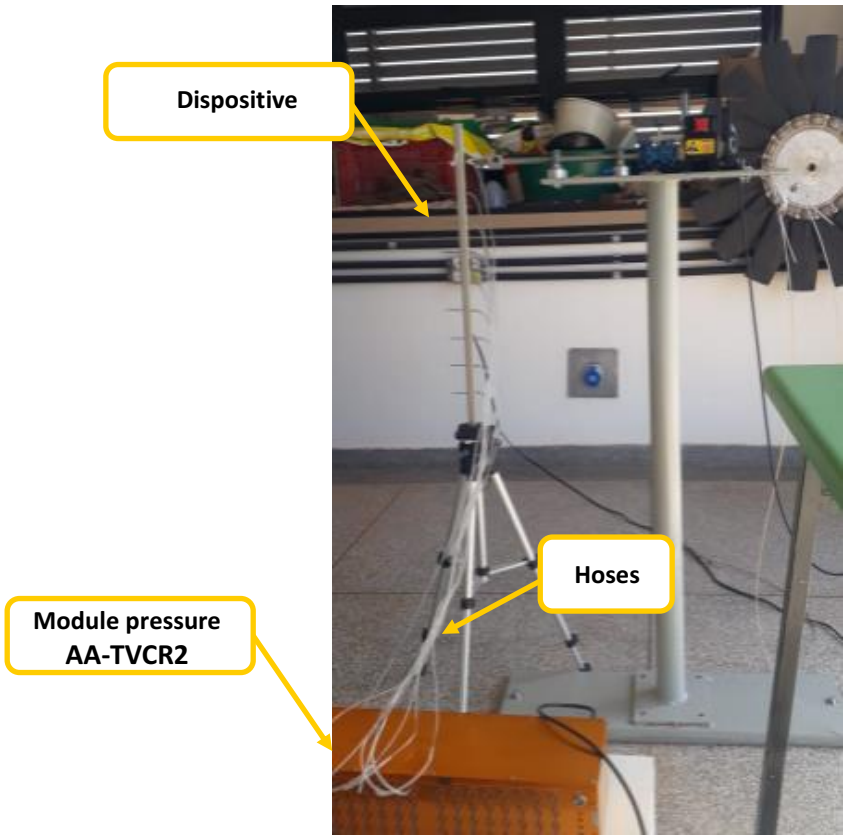


The device was then positioned so that it was in the central position of the test section of the wind tunnel. At each pressure measurement, a measurement was taken at the desired speed to compare the value indicated on the pressure module and on the Kimo, validating if the pressures are correct. With each data collection made in the module's software, the wind tunnel was turned off to avoid possible errors or associated hysteresis. The procedure was repeated for each configuration.

### 5.2.4 Measure of Dynamic Torque

The mechanical power generated by the blade is directly proportional to the torque and angular velocity of the blade. To determine the torque and angular velocity of the blade, the torque transducer is used. In this project, the Torquemaster Magtrol® Model TM 307 was used, whose specifications, according to the manual, is to provide measurement of dynamic torque and propeller speed. Its measurement accuracy is less than $0.1\%$ and has high speed applications up to $50{,}000\,RPM$, much higher than expected in the experiment. The torque transducer is connected to a display that supplies

power to any TM/TMHS/ TMB Transducer and is capable of displaying the torque, speed and mechanical power of the wind turbine.

To measure the correct torque generated by the wind turbine, a braking device was developed. The braking device is used to dampen the rotational energy of the rotating wind turbine. A bicycle brake shoe was used in the experiment to apply a resistive force that allowed dampening the rotational energy, as shown in Figure 51.

**Figure 51.** Experimental wind turbine setup.

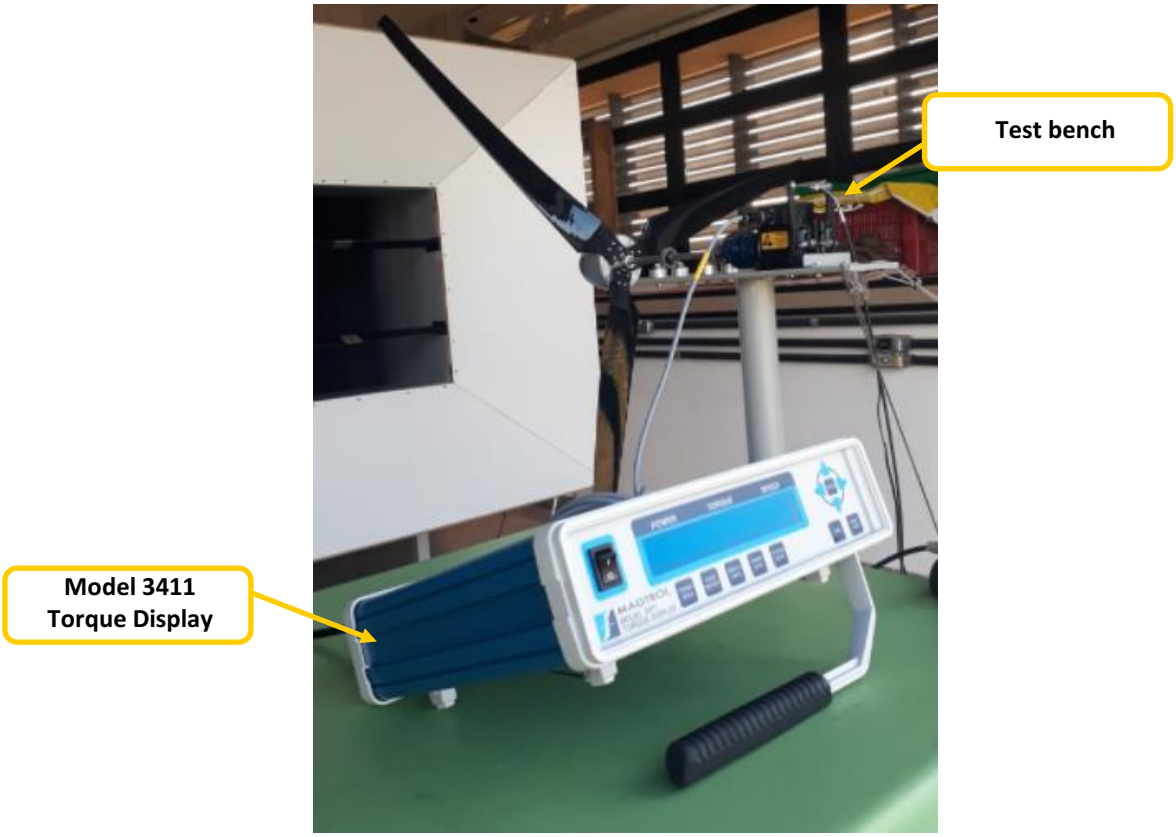

**Figure 52.** Experimental bench wind turbine setup.

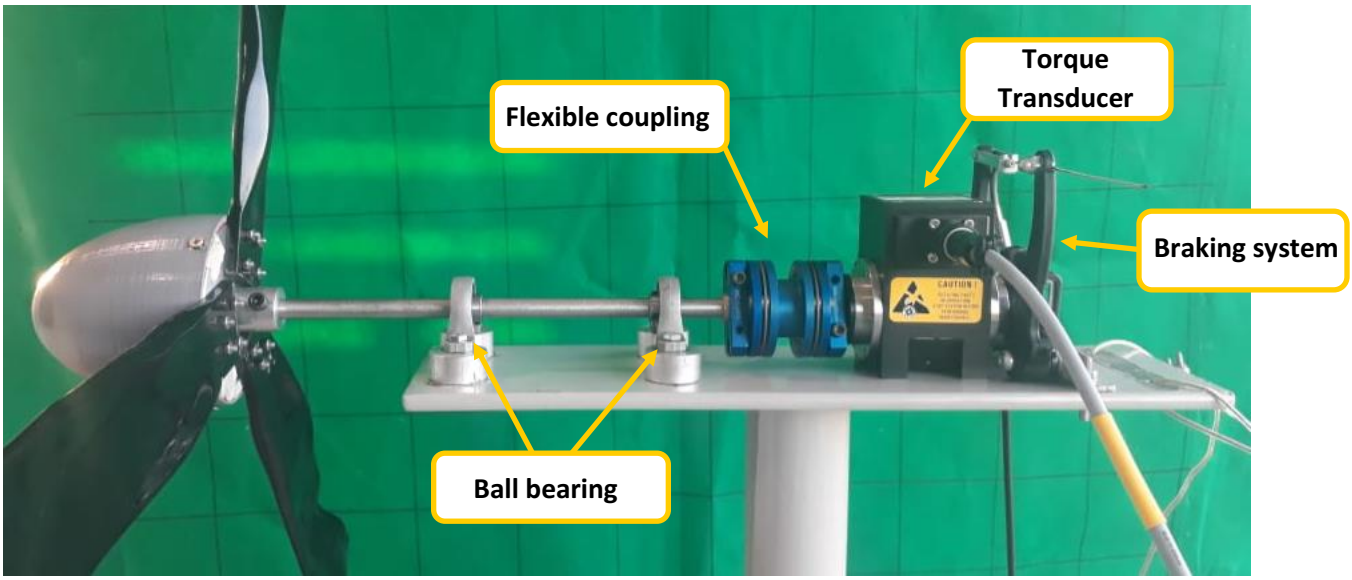


As the fixed-to-axis torquemeter experiment is administered for frequencies from $4\ Hz$ to $28.3\ Hz$, readings are taken by taking the reading on the torquemeter display approximately one minute between measurements. In addition, tests were performed for both the sensitivity of 5N.m/5V and $10\ N.m/5v$. Futhermore, during the experiment, the turbine was operated at constant wind speed, while the speed of rotation was varied to obtain results for different TSR.

Resistive force would be applied until the wind turbine came to a complete stop and torque was recorded. This methodology was repeated three more times and with that the Average Dynamic Torque measured for a specific given frequency and blade configuration was acquired. Thus, the Dynamic Torque is determined for all situations provided for here. The mechanical power generated by the wind turbine is proportional to:

$$P = T\omega \tag{52}$$

where, $T$ is the Torque $(N.m)$ and $\omega$ is the rotational speed $(rad/s)$.

## 5.3 Wind tunnel Speed Errors

The air velocity in the wind tunnel was measured using a to an AA-TVCR2 reference pressure transducer. To verify the readings obtained from the pressure

transducer, the air velocity was also measured with a hot-wire anemometer and an ellipsoidal head Pitot-static tube. The variation in wind tunnel air speed was found to be less than 1%.

# CHAPTER 6

## 6 RESULTS

### 6.1 PRELIMINARY STUDY

The research began in mid 2018, as a theoretical-experimental research, applied to the analysis of airflow in the blades of two small wind turbines (HAWT) with three blades, aiming to obtain the coefficients of power, torque, shaft rotation and other parameters that allow the characterization of the performance of a wind turbine. This work was presented at the 25° COBEM – International Congress of Mechanical Engineering. The results can be seen in the Appendix C.

The coordinates of the winged edges of the seed were plotted using *GetData*®. Turbine geometry was converted to stereolithography (STL) format using 3D modeling software. Then, two small-scale models were manufactured by a deposition process using a 3D *MakerBot*® Replicator Z18: an initial simplified prototype of a dynamic size model of a seed for wind tunnel testing is provided and compared to a reference model of blades, rotor and hub and simplified fairing - Figure 53.

**Figure 53.** Final scaled model prototypes (reference and Q. Multiflora's blades).

First, it was necessary to analyze the velocity distribution in the tunnel cross section with the aid of a wire anemometer. With the speed profile of both models, the static torque of the prototype is determined by means of a developed equipment coupled to the equipment axis, which registers all readings for a speed range from $2\ m/s$ to $10\ m/s$. A phototachometer was used to measure the rotation of the free rotating model against the flow. With the data obtained, the static torque curve and the RPM curve as a function of incident speed were determined.

Through the experimental determination of the incident velocity profile and the velocity profile on the aerodynamic runway of each one, the flow was determined and the power extracted by the rotors in free rotation was evaluated.

A DANTEC Dynamics Streamline Pro anemometer with a 1D hot wire probe (55P11) was used to produce velocity profiles upstream and downstream in the model. In addition, a Pitot tube was placed on the roof of the test section and a digital manometer displayed the free flow velocity. The velocity indication was used to define the stagnation of the free global flow and initiate the acquisition of the anemometer.

Finally, a bench was developed to measure the performance of wind turbines in scale, so that the blades were easily coupled and uncoupled from the hub - Figure 54.

**Figure 54.** Bench for measuring performance of wind turbines at scale.

Figure 55 illustrates the rpm curves for the reference and *Q. Multiflora* geometries. The results showed that the seed geometry capacity is superior to the reference, since the entire set of flows was superior to the conventional configuration. It is important to

point out that the angle of incidence of the Multiflora blade was not properly investigated. In this way, the *Q. Multiflora* blade was made in a position relatively close to $4°$ in the cube. However, it cannot be said that this is the best assembly configuration in order to obtain the best aerodynamic response from the new geometry.

**Figure 55.** RPM for prototypes at different wind speeds.

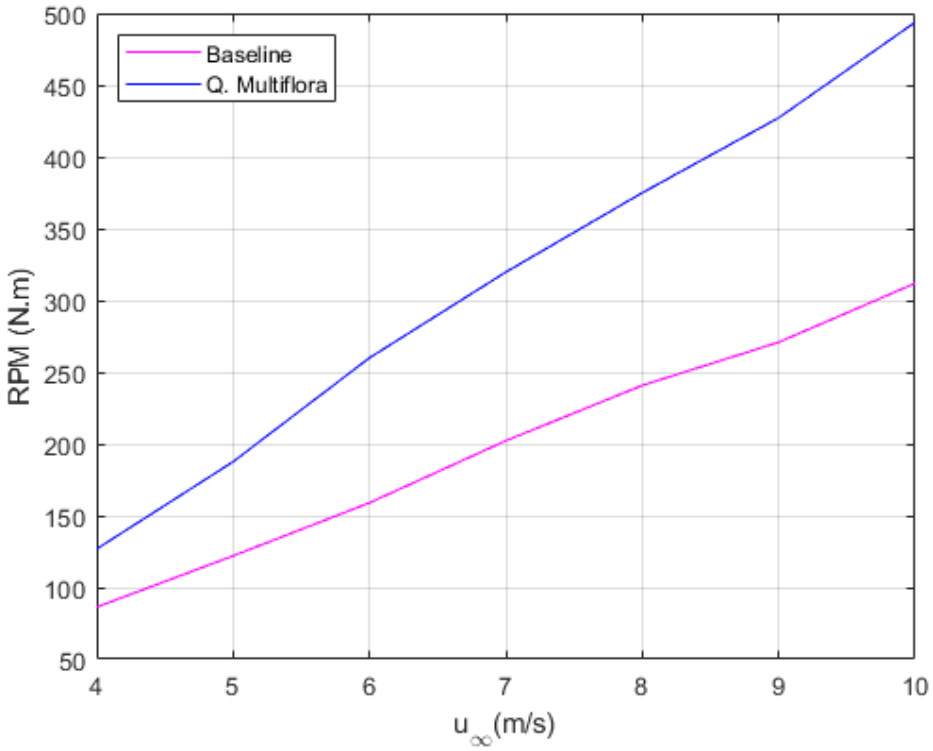


A static torque measurement method was developed, which was previously calibrated before the measurements, withless than $10\%$ of maximum error. The evaluation of static torque was performed with variation in the frequency of the electric motor fan from $4$ to $10\ m/s$, with increments of $1\ m/s$. Tests with the prototypes were carried out using a comparative data collection system. Figure 56 shows the static torque curve, with the same range. The results obtained point to a good relationship between angular velocity and torque for the *Q. Multiflora*-based design.

**Figure 56.** Static torque for the HAWT prototypes for different wind speeds.

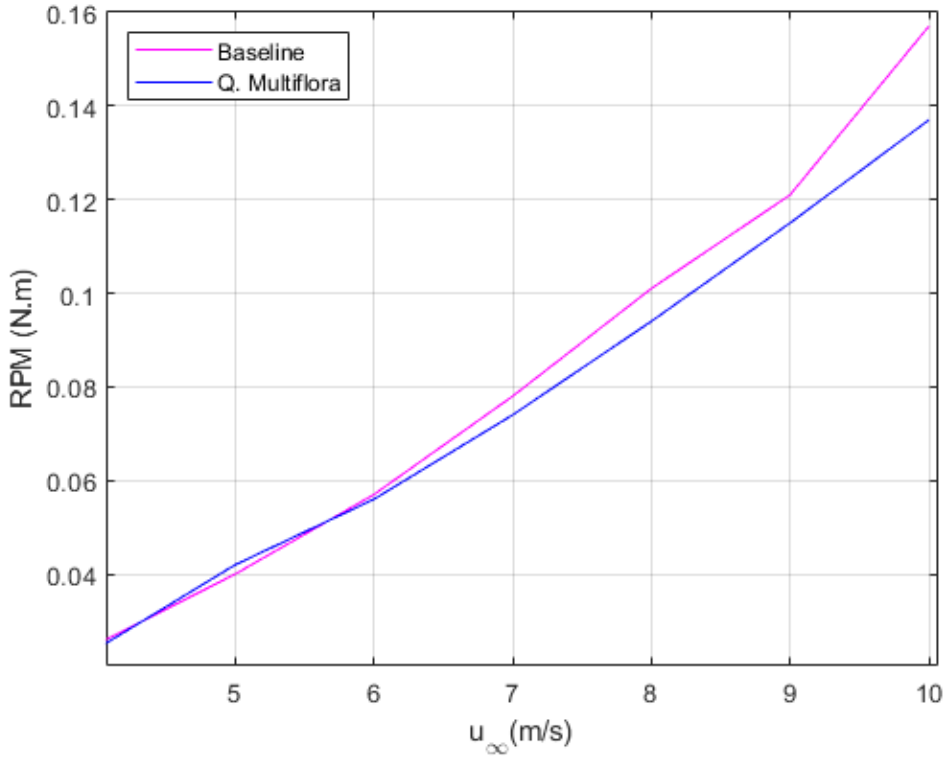


## 6.2 TEST CONDITIONS

The experiments were performed on a day that the ambient temperature was 25°C what correspond to a $\mu = 15.565x10^{-6}\ m^2/s$. The data about environmental conditions is important to calculate the Reynolds number and its corresponding Mach number at which the experiment was carried out. To calculate them, the equations (48) and (49) were used. In this case, the characteristic linear dimension used to obtain the Reynolds number was the blade lenght. Thus, substituting the linear dimension of the 1.2 meter characteristics and the kinematic viscosity, the Reynolds and Mach number of each velocity of each flow can be seen in the following table:

**Table 5.** Wind tunnel speed and their respective Reynolds and Mach numbers.

| Velocity ($m^2/s$) | Reynolds (Re) | Mach (M) |
|---|---|---|
| 4 | 360192.74 | 0.0138 |
| 6 | 540289.11 | 0.0208 |
| 8 | 720385.48 | 0.0277 |
| 10 | 900481.85 | 0.0346 |
| 12 | 1080578.22 | 0.0415 |
| 14 | 1260674.59 | 0.0484 |
| 16 | 1440770.96 | 0.0554 |

### 6.2.1 Velocity profile acquisition

The purpose of this section is to compare velocity curves for each $u_\infty$ in coincident graphs. Since the wind tunnel is symmetrical, as shown in Figure 57, it is possible to bounce the measurements up. After the readings were taken, the velocity data were entered in *Matlab*® and, with that, the transverse profile in the test section of the wind tunnel is obtained. This speed profile is determined for wind tunnel fan motor operating frequencies from 10 to 28.3 Hz as shown in Table 6 graphical results of these analyzes can be seen in the figure below:

**Figure 57.** Velocity profiles plot.

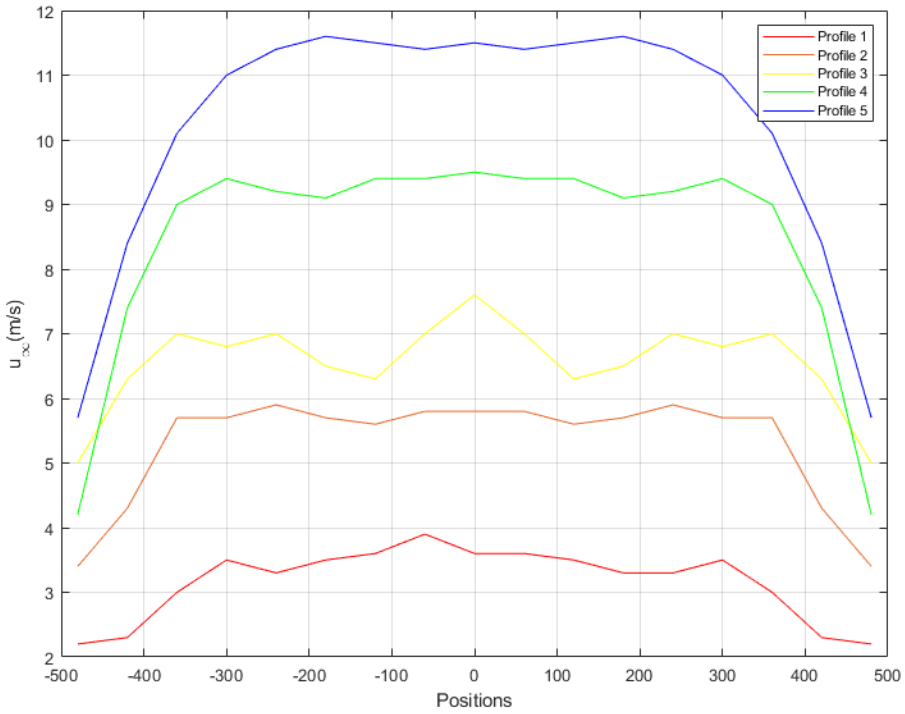

**Table 6.** Data collected to plot speed profiles.

| V (m/s) | 4 | 6 | 8 | 10 | 12 |
|---|---|---|---|---|---|
| **Frequency (Hz)** | 10 | 15.2 | 19.2 | 24.3 | 28.3 |
| | $U_\infty\ (m/s)$ | | | | |
| **P1** | 2.2 | 3.4 | 5 | 4.2 | 5.7 |
| **P2** | 2.3 | 4.3 | 6.3 | 7.4 | 8.4 |
| **P3** | 3 | 5.7 | 7 | 9 | 10.1 |
| **P4** | 3.5 | 5.7 | 6.8 | 9.4 | 11 |
| **P5** | 3.3 | 5.9 | 7 | 9.2 | 11.4 |
| **P6** | 3.3 | 5.7 | 6.5 | 9.1 | 11.6 |
| **P7** | 3.5 | 5.6 | 6.3 | 9.4 | 11.5 |
| **P8** | 3.6 | 5.8 | 7 | 9.4 | 11.4 |
| **P9** | 3.9 | 5.8 | 7.6 | 9.5 | 11.5 |
| **P10** | 3.6 | 5.8 | 7 | 9.4 | 11.4 |
| **P11** | 3.5 | 5.6 | 6.3 | 9.4 | 11.5 |
| **P12** | 3.3 | 5.7 | 6.5 | 9.1 | 11.6 |
| **P13** | 3.3 | 5.9 | 7 | 9.2 | 11.4 |
| **P14** | 3.5 | 5.7 | 6.8 | 9.4 | 11 |
| **P15** | 3 | 5.7 | 7 | 9 | 10.1 |
| **P16** | 2.3 | 4.3 | 6.3 | 7.4 | 8.4 |
| **P17** | 2.2 | 3.4 | 5 | 4.2 | 5.7 |

Note that all curves have well-defined and similar behavior regardless of the speed set in the wind tunnel. The first characteristic observed is the shape similar to an "M", which suggests that in the central region of the body in an approximate extension between points 4 and 14 of the x-axis reference, there is a more stable flow region, which quickly after this extension takes on another characteristic, that of a progressive increase in the measured velocity, with the change in the horizontal position. Suggesting the presence of a more active and complex flux field in this region.

The wind tunnel velocity profile is somewhat blunt, showing the highest airflow velocities in the center of the channel, and a speed variation, between the highest and the lowest, of $1.7\ m/s\ (10\ Hz)$, $2.4\ m/s\ (15.2\ Hz)$, $2.6\ m/s\ (19.2\ Hz)$, $5.3\ m/s\ (24.3\ Hz)$, $5.8\ m/s\ (28.3\ Hz)$, which for practical purposes, can caused some damage to the observed data, although the prototype remained in the area of more constant speeds (center of the channel). For this reason, improvements must be made to improve the channel and wind tunnel and stabilize the flow in all positions of the tunnel cross section.

## 6.1 PERFOMANCE

To the detriment of laboratory restrictions and the lack of time caused by the COVID-19 pandemic that we are experiencing in 2020 and 2021, much of the project was

carried out remotely. Therefore, there was not enough time to deepen the studies, repeat tests and any corrections and adjustments to the experiment.

Thus, the results to be presented were influenced by the experimental configuration and possible sensitivity to the test parameters. However, the results will be discussed based on the theory and proposition of corrections, adjustments and future work will be considered in this study.

Furthermore, it is important to highlight that this is the first study to adopt a biomimetics solution carried out at LAEX, which will serve as a learning curve for future work.

### 6.1.1 Experimental analyses

During the experimental test in a wind tunnel, the non-linear variation of the data collected in the three configurations was notable, making it impossible to draw performance curves. It is believed that the measurement errors are linked to friction in the bearing used in the experiment, as well as to the braking mechanism. However, the brake system shoe did not provide good grip.

To the detriment of the current world scenario, due to the impact of COVID-19, the occasional difficulties in developing a purely experimental work during the lockdown and limitations of access to the laboratory, other tests of bench configurations became unfeasible. Therefore, in future research, we will seek to replace the bearing with a more suitable one and develop a more efficient braking system.

However, it is possible to plot the curve of Wind Power vs wind speed, where it is possible to visualize the expected powers in the working range we are dealing with. So, using equation (16) it was possible to plot the following graph:

**Figure 58.** Expected power curve.

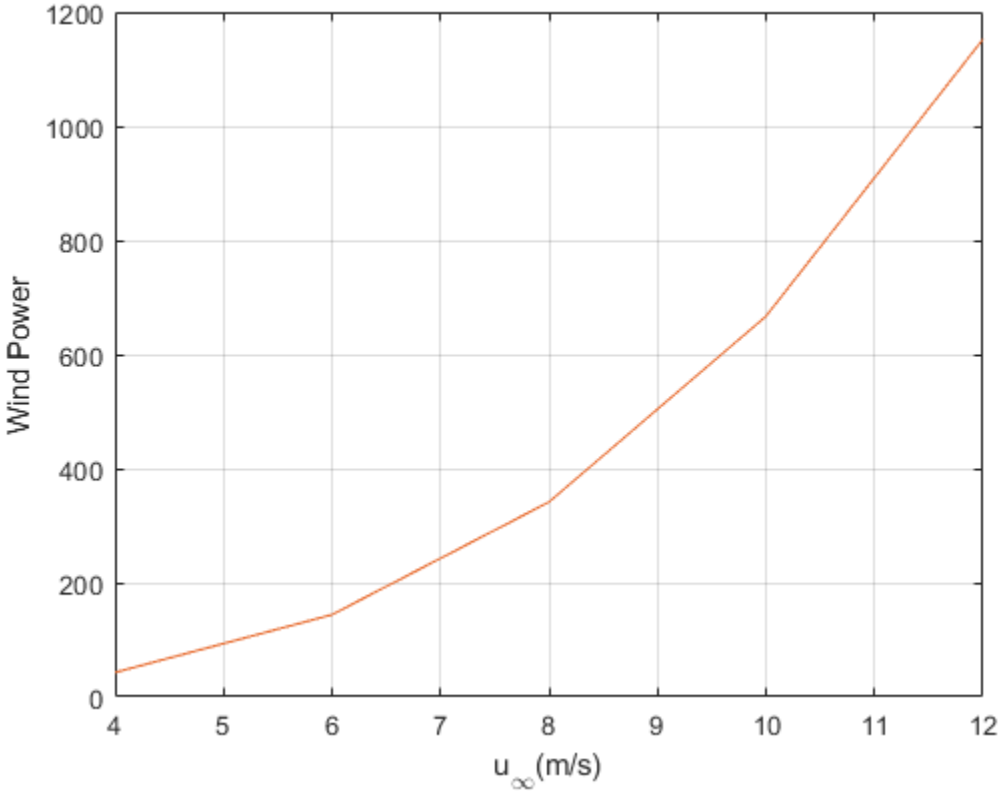

# CHAPTER 7

## 7 CONCLUSIONS & RECOMMENDATIONS FOR FUTURE WORK

Generally, wind turbine blades are shaped to generate maximum energy from the wind with minimal construction cost. However, wind turbine blade manufacturers are always looking to develop a more efficient blade design. Constant improvements in wind blade design have produced new wind turbine designs that are more compact, quieter and capable of generating more energy with less wind.

The design of wind turbine blades is crucial to meet spectations. The innovations and new technologies used to design wind turbine blades are constantly being innovated to improve their performance, efficiency and energy production.

Three sets of full-scale HAWT blades have been designed and manufactured, with assorted blade tips approximately $1.2$ meter in diameter. The series of tests was carried out in the TV-60 wind tunnel to assess the performance of the turbine blades and their power generation capacity. The turbine blades that were developed and investigated in this research have similar solidity, but are geometrically different. A reference was used as a reference to assess the performance of both biomimetic blades.

Analyzing the data collected in the three configurations, it was noticed that despite the non-linearity of the data, which made it impossible to determine important aerodynamic characteristics of the project such as the power curve, it was possible to make important improvements in crucial points.

The first biomimetic slide was obtained by a coordinate system, having many geometric variations, while the current one was obtained by 3D scanning, providing a faithful geometry to a sample collected for the study.

In addition, due to the limitation on the size of the wind tunnel test section, the first version had a limitation regarding tip losses. To reduce this, it was necessary to increase the turbine diameter and, consequently, the size of the test section. For this, a diffuser coupled to the tunnel was built, as discussed in section 5.2.1.

The first bench that had a simple torque measurement system was rebuilt to include a torque transducer and braking system for more accurate data measurement.

The continuation of this work should have more efficient braking apparatus and bearings for new measurements, making it possible to trace its power and torque curve. In addition, it is planned in the future to carry out a numerical analysis in CFD, simulating the model configurations under the same environmental conditions as the tests. With the

numerical results, it is possible to understand what kind of influence, positive or negative, the new geometries have on the aerodynamic forces, which complements the analysis of this work.

# REFERENCES


ABEEÓLICA. Associação Brasileira de Energia Eólica. ABEEÓLICA, 2018. Disponível em: <http://abeeolica.org.br/>. Acess in: 31 Mar. 2021.

AeroAlcool. AA-TVCR2: Módulo de Pressão 64x. Disponível em: <http://www.aeroalcool.com.br/index.php/acessorios/32-gallery/acessorios/128-aa-tvcr2>. Acess in 05 Jun. 2021

Associação Brasileira de Energia Eólica (São Paulo, Brasil). Ventos ajudam Brsil a diversidicar matriz energética. Disponível: http://www.abeeolica.org.br/zpublisher/materias/Noticias.asp?id=19385. Acesso em: 15 de jun. 2021.

Afjeh, A., Keith, T. G.: A Simple Computational Method for Performance Prediction of Tip-Controlled Horizontal Axis Wind Turbines, Journal of Wind Engineering and Industrial Aerodynamics, Vol.32, 1989.

Airfoiltools. Airfoil Database. 2021. SG6051 AIRFOIL (sg6051-il). [online] Airfoiltools.com. Available at: < http://airfoiltools.com/airfoil/details?airfoil=sg6051-il > [Accessed 25 May 2017].

Ali, A M. Aerodynamic optimization of small scale horizontal axis wind turbine blades. Bsc in Aerospace engineering. RMIT University, Melbourne, Australia, 2014.

Alves, A. S. G. Análise do Desempenho de Rotores Eólicos de Eixo Horizontal. Dissertação de Mestrado, Universidade Federal do Pará, Brasil, 1997.

Anderson JW, Brulle RV, Birchfield EB, Duwe WD. McDonnell 40 kW Giromillwind systemephase I: design and analysis. RFP-3032/1. McDonnell AircraftCompany; 1979.

Augspurger, Carol K. "Morphology and Dispersal Potential of Wind-Dispersed Diaspores of Neotropical Trees." American Journal of Botany 73, no. 3 (1986): 353-63. Accessed June 11, 2021. doi:10.2307/2444078.

Associação Brasileira de Energia Eólica (São Paulo, Brasil). Nordeste desponta como potencial de energia eólica. Disponível: http://www.abeeolica.org.br/zpublisher/materias/Noticias.asp?id=19455. Acesso em: 15 de jun. 2021.

AWEA.2010 Small Wind Turbine Global Market Study; AWEA: Washington, DC, USA, 2010.

DOE.2017 Wind Technologies Market Report; DOE: Washington, DC, USA, 2018.

Azuma, A. and Okuno, Y. (1987) Flight of a Samara, Alsomitra macrocarpa. Journal of Theoretical Biology, 129, 263-274. https://doi.org/10.1016/S0022-5193(87)80001-2.

Betz, “A. Windenergie und Ihre Ausnutzung durch Windm¨ullen”, Gottingen, Germany, 1926.

Burton, T. et al. Wind Energy Handbook. Segunda edição. ed. West Sussex: [s.n.], 2001.

Burton T., Sharpe D., Jenkins N., Bossanyi E., “Wind Energy Handbook”, John Wileyand Sons, 2001

Castaignet, D.; Barlas, T.; Buhl, T.; Poulsen, N.K. Full-scale test of trailing edge flaps on a Vestas

V27 windturbine: Active load reduction and system identification. Wind Energy2014,17, 549–564.

Chu, Y. J., & Chong, W. T. (2017a). A Biomimetic Wind Turbine Inspired by Dryobalanops Aromatica Seed: Numerical Prediction of Rigid Rotor Blade

Performance with OpenFOAM®. Computers & Fluids, 159, 295-315.

Darrieus GJM. Turbine having its rotating shaft traverse to theflow of thecurrent, US Patent No. 1,835,018; 1931.

Dantec Dynamics A/S. MiniCTA Anemometer Package How to get started -a quick Guide. 2004.

Desenfans, P. The aerodynamics of a falling maple seed. Institutional Repository of Leibniz University of Hannover. 2019.

Detanico, F. B. Sistematização de princípios de solução da natureza para apli-cação no processo criativo de projeto de produtos. Universidade Federal do Rio Grande do Sul. Porto Alegre, p. 191. 2011.

BRASIL. “Concede isenção do ICMS nas operações com equipamentos e componentes para o aproveitamento das energias solar e eólica. Diário Oficial da República Federativa do Brasil. 18 dez. 1997, Sec. 1, p. 174,” Rio de Janeiro, 2002.

Cayley, G. Sketch of a dolphin, and design for a solid of least resistance based on it (undated). Gibbs-Smith Sir George Cayley’s Aeronautics.1855.

Chen, T. & Liou, L.2011 Blockage corrections in wind tunnel tests of smallhorizontal-axis wind turbines. Experimental Thermal and Fluid Science35, 565–569.

Energia eólica chega a 18 GW de capacidade instalada no Brasil. Canal Energia, 2021. <https://www.canalenergia.com.br/noticias/53163929/energia-eolica-chega-a-18-gw-de-capacidade-instalada-no-brasil#:~:text=Energia%20e%C3%B3lica%20chega%20a%2018%20GW%20de%20capacidade%20instalada%20no%20Brasil,-Dados%20de%20fevereiro&text=A%20energia%20e%C3%B3lica%20acaba%20de,e%20mais%20de%208.300%20aerogeradores.> Acesso em: 28 de maio de 2021

Clausen, FD; Wood, DH. Research and development issues for small wind turbines, Renew. Energy. 16 (1999) 922–927. doi:10.1016/S0960-1481(98)00316-4.

Fragola, L J. Abundância e diversidade de herbívoros em Peixotoa tomentosa A. Juss. (Malpighiaceae) no Cerrado e sua relação com formigas visitantes de nectários extraflorais. 31 f. Trabalho de Conclusão de Curso (Graduação em Ciências Biológicas) – Universidade Federal de Uberlândia, Uberlândia, 1999.

Fish, F. E., Howle, L. E. and Murray, M. M. 2008. Hydrodynamic flow control in marine mammals; Integrative and Comparative Biology 211: 1859-1867.

Gaitan-Aroca, J.; Sierra, F.; Castellanos Contreras, J.U. Bio-Inspired Rotor Design Characterization of a Horizontal Axis Wind Turbine. Energies 2020, 13, 3515. https://doi.org/10.3390/en13143515

Glauert H., “Airplane Propellers: Aerodynamic Theory”, (ed. W. F. Durand), Springer.

Glauert, H. The elements of Aerofoil and AirscrewTheory. Cambridge University Press, London, UK, 1926

Impressão 3D Fácil. Conheça os diferentes tipos de materiais para impressão 3D FDM. 1 dez 2015. Disponível em: https://www.impressao3dfacil.com.br/conheca-os-diferentes-tipos-de-materiais-para-impressao-3d-fdm/. Acesso em: 09 jun. 2021.

Green, D S. The terminal velocity and dispersal of spping samaras. Armer. J. Bot. 67: 1218-1224

International Energy Agency.Key World Energy Statistics; IEA: Paris, France, 2017.

Gould, J., Fiddes, S. P.: Computational Methods for the Performance Prediction of HAWTs, Journal of Wind Engineering and Industrial Aerodynamics, Vol.39, 1992.

Hau, E. (2005). Wind Turbines Fundamentals Technologies Application Economics (1st ed.) Germany: Springer.

Krogstad, P. Å., & Lund, J. A. (2012). An Experimental and Numerical Study of the Performance of a Model Turbine. Wind Energy, 15, 443-457.

Lentink, D., Dickson, W. B., van Leeuwen, J. L., & Dickinson, M. H. (2009). Leading-Edge Vortices Elevate Lift of Autorotating Plant Seeds. Science, 324(5933), 1438–1440. doi:10.1126/science.1174196

Manwell, J., McGowa, J., Rogers, A. (2009). Wind Energy Explained Theory Design and Application (2nd ed.). UK: John Wiley & Sons.

Lentink, D; Dickson, WB; van Leeuwen, JL; Dickinson, MH. Leading-Edge Vortices Elevate Lift of Autorotating Plant Seeds, Science 324, 1438-1440 (2009).

Ledoux J, Riffo S, Salomon J. Analysis of the Blade Element Momentum Theory.2020. hal-02550763

LLGAYER, R. Formas naturais e estruturação de superfícies mínimas em arquite-tura. Universidade Federal do Rio Grande do Sul. Porto Alegre, p. 157. 2009.

Magdi Ragheb and Adam M. Ragheb (July 5th 2011). Wind Turbines Theory - The Betz Equation and Optimal Rotor Tip Speed Ratio, Fundamental and Advanced Topics in Wind Power, Rupp Carriveau, IntechOpen, DOI: 10.5772/21398. Available from: <https://www.intechopen.com/books/fundamental-and-advanced-topics-in-wind-power/wind-turbines-theory-the-betz-equation-and-optimal-rotor-tip-speed-ratio>. Acesso em: 10 abr. 2021.

Manwell, J. F., McGowan, J. G., Rogers, A. L.: Wind Energy Explained; Theory, Design and Application, John Wiley & Sons Ltd, 2002.

Mishnaevsky Jr, L., Freere, P., Sinha, R., Acharya, P., Shrestha, R., &Manandhar, Pushkar. (2011). Small wind turbines with timber blades for developing countries: Materials choice, development, installation and experiences. Renewable Energy, 36(8), 2128-2138

Mundim, J. P. Estudo experimental do escoamento ao redor de cilindros de base quadrada com diferentes razões de aspecto montados sobre uma superfície. 2019. Trabalho de Conclusão de Curso, Universidade Federal de Uberlândia, Uberlândia.

Nathan, R. (2006) Long-Distance Dispersal of Plants. Science, 313, 786-788. https://doi.org/10.1126/science.1124975.

Neto, J. B. Estudo de elemento da natureza para aplicação em design: Biomime-tização da estrutura de ninhos de cacicus haemorrhous. Universidade Federal do Paraná. Curitiba, p. 194. 2013

Neill, S. P., & Hashemi, M. R. (2018). Offshore Wind. Fundamentals of Ocean Renewable Energy, 83–106. doi:10.1016/b978-0-12-810448-4.00004-5.

New, D. T. H., & Ng, B. F. (Eds.). (2020). Flow Control Through Bio-inspired Leading-Edge Tubercles. doi:10.1007/978-3-030-23792-9

Novaes, L R. Padrões fenológicos e dispersão de siásporos de espécies anemocóricas representativas do cerrado. Uverlândia, MG, 2020. Instituto de Biologia UFU. Tese de mestrado.

Pawlyn, M., 2011, “Biomimicry in Architecture”,RIBA Publishing,London

Pandey, M. M., Pandey, K. P., Ojha, T. P.: An Analytical Approach to Optimum Design and Peak Performance Prediction for Horizontal Axis Wind Turbines, Journal of Wind Engineering and Industrial Aerodynamics, Vol.32, 1989.

Peres, M K. Estratégias de dispersão de sementes no bioma cerrado: considerações ecológicas e filogenéticas. Brasília, DF, 2016. Universidade de Brasilia. Tese de doutorado.

Practical Action, “Wind for electricity generation", Internet Survey, Visited on 25th of March (2012). URL:http://www.cd3wd.com/cd3wd_40/CD3WD/Technical%20Briefs/Energy%20Technology%20Use/KnO-100174_wind_for_electricity_generation.pdf

Porté-Agel, F.; Bastankhah, M.; Shamsoddin, S. Wind-Turbine and Wind-Farm Flows: A Review;

RenewableUK.Small and Medium Wind Strategy; RenewableUK: London, UK, 2014.

R. Bennett and J. Elton, History of corn milling, Vol. 2, Simpkin, Marshall and Company Ltd, London, 1899.

Ramos, J. A biônica aplicada ao projeto de produtos. Universidade Federal de San-ta Catarina. Florianópolis, p. 56. 1993

RAMOS, J. Alternativas para o projeto ecológico de produtos. Universidade Federal de Santa Catarina. Florianópolis, p. 152. 2001

Reis, T. H. Desenvolvimento de texturas cm base em estudos biomiméticos acerca dos pássaros da espécie sicalis flaveola (canário-da-terra) associados ao design emocional. Universidade Federal do Rio Grande do Sul. Porto Alegre, p. 101. 2013

Rosa, L. C. Desenvolvimento de carenagem para miniveículo visando eficiência energética com base na biônica. Universidade Federal do Rio Grande do Sul. Porto Alegre, p. 114. 2013.

Salvador, R. J. Metodologia biônica em dobradiça de móveis. Universidade Fede-ral do Rio Grande do Sul. Porto Alegre, p. 122. 2003.

Silveira, J. P. An experimental study of the aerodynamic characteristics of an aircraft model with canard-wing configuration. 2017. 77p. Graduation Project, Federal University of Uberlândia, Uberlândia, Brazil.

It is speculated that the origin of the first wind rotors in classical Greece, Babylon, early Gaul and Saxon England, however there are no references to wind-powered machines in reliable records of ancient and medieval periods (Bennett and Elton, 1899). Shahan (2014), defines that the use of wind for mechanical and electrical purposes is dated in

Schubel, P.J.; Crossley, R.J. Wind turbine blade design. Energies2012,5, 3425–3449.

Springer: Dordrecht, The Netherlands, 2019; Volume 174.

Spera, D. A.: Wind Turbine Technology, ASME Press, 1998.

Tummala, A., Velamati, R. K., Sinha, D. K., Indraja, V., & Krishna, V. H. (2016). A review on small scale wind turbines. Renewable and Sustainable Energy Reviews, 56, 1351–1371. doi:10.1016/j.rser.2015.12.027.

Sette, T. C. C. Desenvolvimento de uma proposta de indicadores para avaliação do

desempenho ambiental dos processos produtivos industriais sob a ótica da biomimética. Universidade Vale do Rio dos Sinos. São Leopoldo, p. 142. 2010.

Sumner, J.; Watters, C.S.; Masson, C. CFD in wind energy: The virtual, multiscale wind tunnel. Energies 2010,3, 989–1013

Sirohi, J. (2013) Microflyers: Inspiration from Nature. Proceedings of SPIE—The International Society for Optical Engineering, 8686, 1-15. https://doi.org/10.1117/12.2011783

Souza, S. F. “Análise de Turbinas Eólicas de Eixo Vertical (Darrieus e Lenz2) e Horizonal para o Dimensionamento de Geradores Elétricos. Campo Grande, MS, 2018.

Storm, R. “Maple Seed” Helicopters. Nasa, 2021. Disponível em: < https://www.grc.nasa.gov/www/k-12/TRC/Aeronautics/Maple_Seed.html>. Acesso em 05 de Jul. 2021.

Taveiros, F. E. V., Barros, L. S., & Bezerra Costa, F. (2013). Wind turbine torque-speed feature emulator using a DC motor. 2013 Brazilian Power Electronics Conference. doi:10.1109/cobep.2013.6785159

van Nierop, E.A.; Alben, S.; Brenner, M.P. How bumps on whale flippers delay stall: An aerodynamic model.Phys. Rev. Lett.2008,100.

Usher, A P. A History of Mechanical Inventions, New York [etc.: McGraw-Hill Book, 1929.

Vincent, J. F., Bogatyrev, O. A., Bogatyrev, N. R., Bowyer, A., & Pahl, A. (April 2006). Biomimetics-Its Practice & Theory. Journal of the Royal Science Interface.

Vogel, S. 1981. Life in moving fluids. Willard Grant Press, Boston.

Werle, M.2009Passing Through the Wind Turbine Thrust Singularity. FloDesignInc. Wilbraham, MA 01095.

Zari, M. P. (2007). Biomimetic Approaches to Architectural Design for Increased Sustainability. Sustainable Building Conference.Auckland: [Personal communication].

Zhiquan, Y., Zhaoxue, C., Jingyi, C., Shibao, B. Aerodynamic Optimum Design Procedure and Program for the Rotor of a Horizontal-Axis Wind Turbine, Journal of Wind Engineering and Industrial Aerodynamics, Vol.39, 1992.

# APPENDIX A – TECHNICAL DRAWINGS OF WIND TURBINE

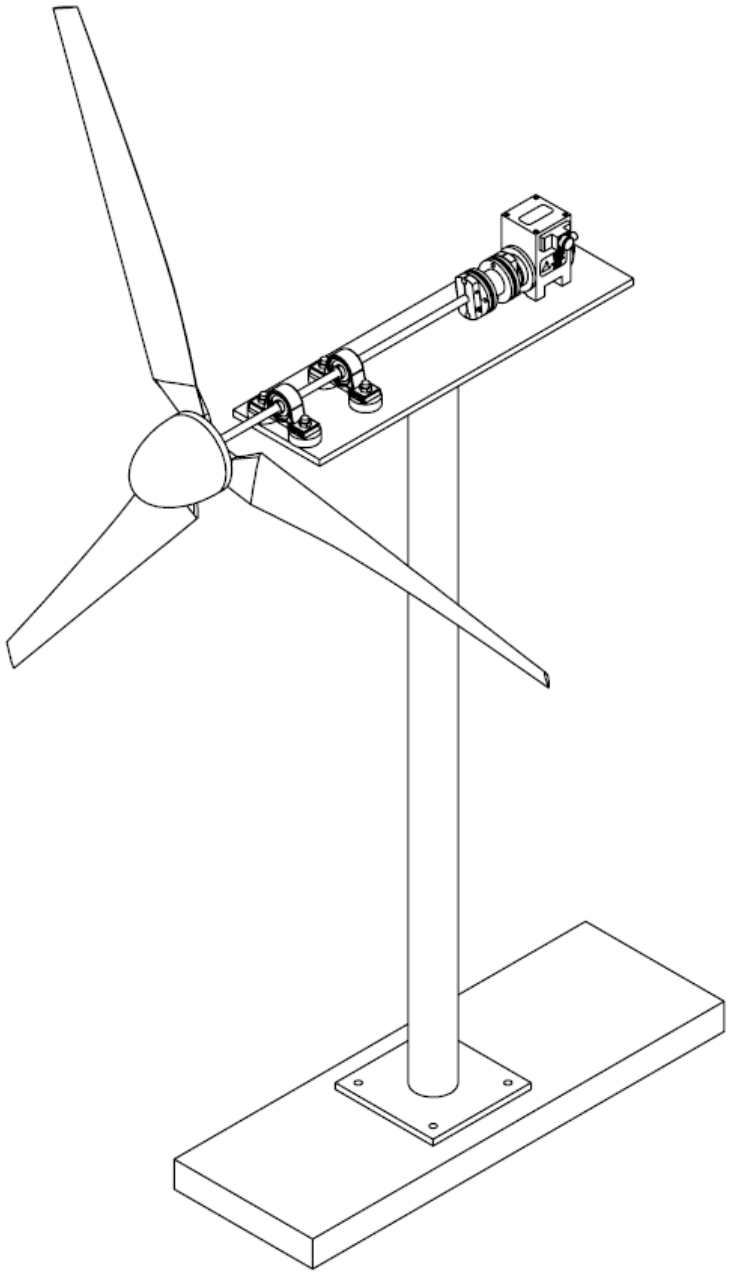

**Figure 59:** Full Scale Wind Turbine Isometric View.

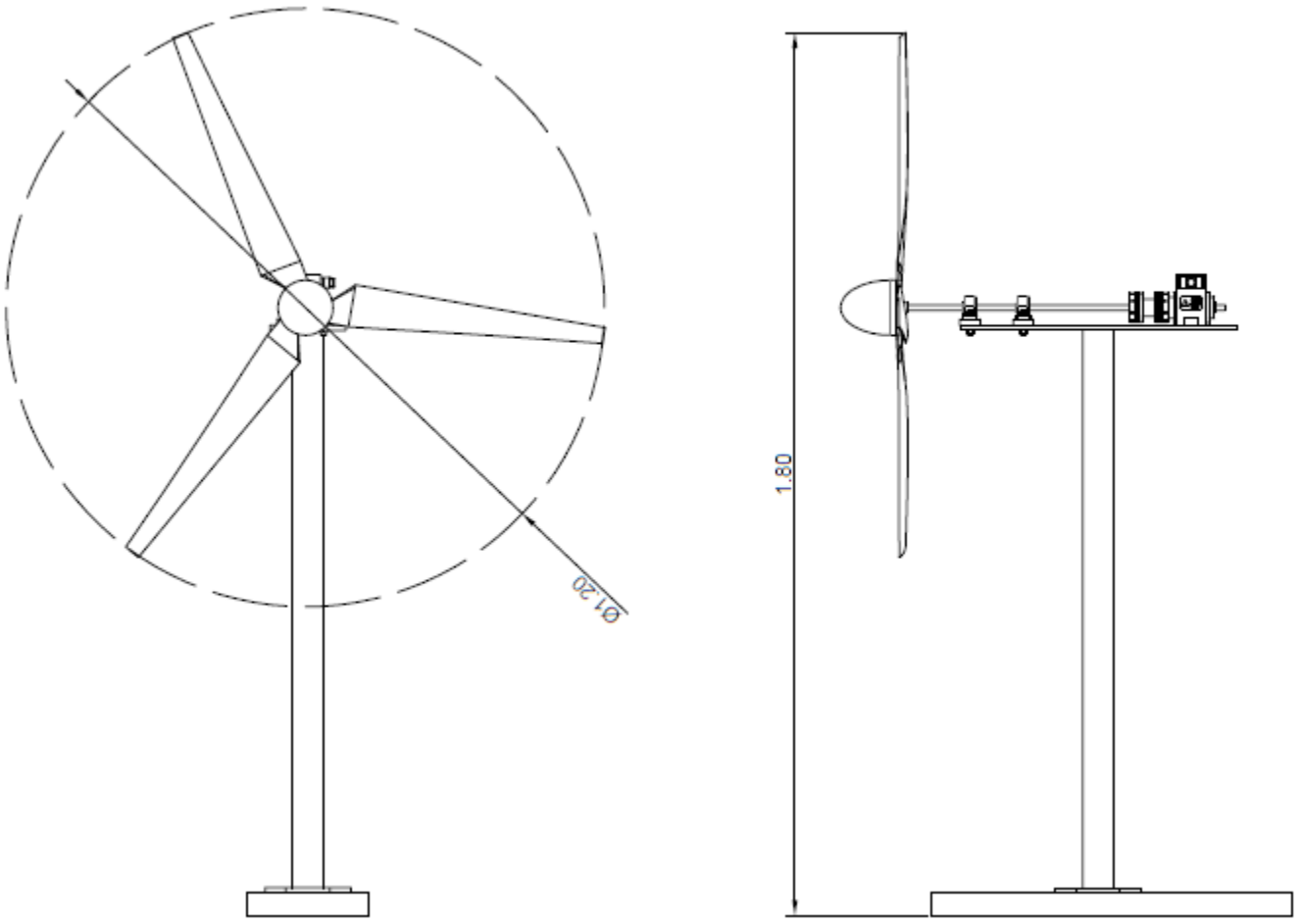


*(a)* *(b)*

**Figure 60.** Wind turbine assembly (a) Frontal view (b) Side view

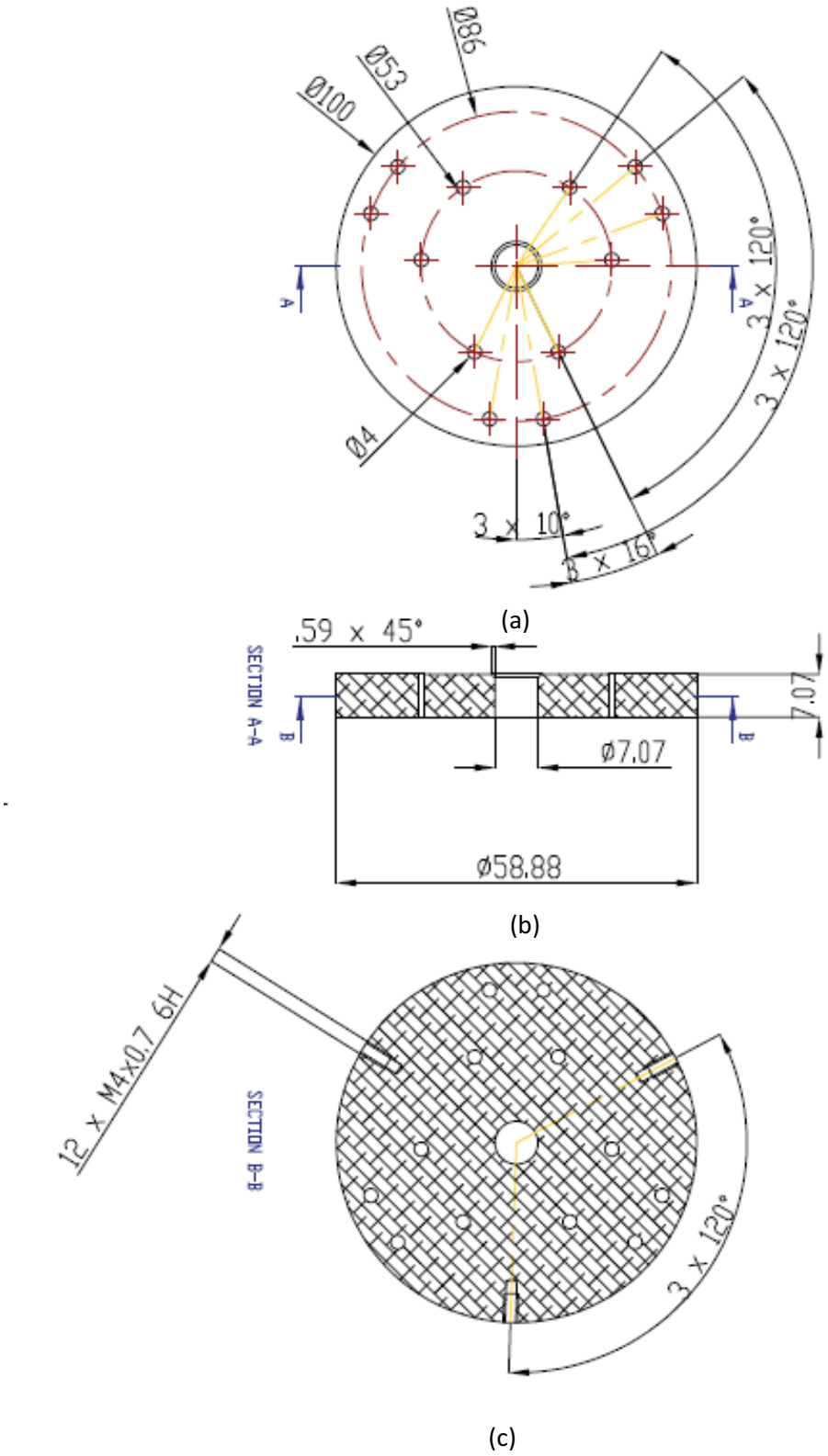


**Figure 61.** Wind turbine hub (a) front view (b) section view A-A(c) section view B-B.

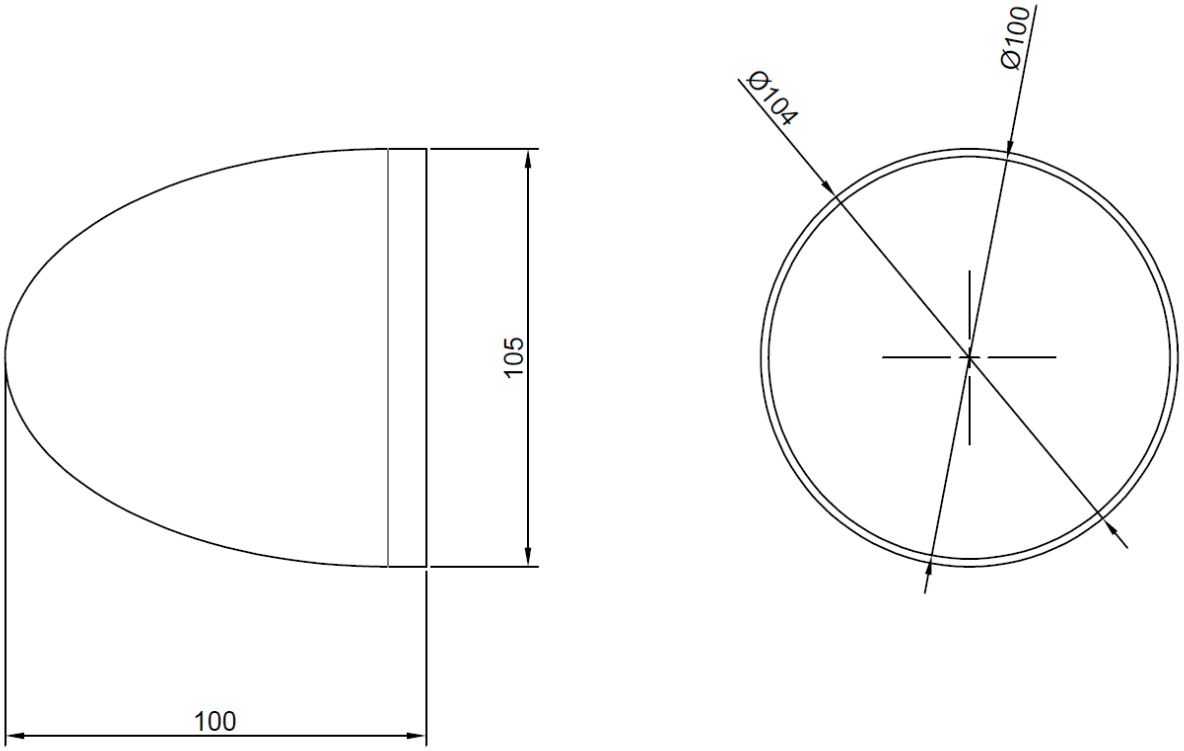


**Figure 62.** Geometry of nose cone.

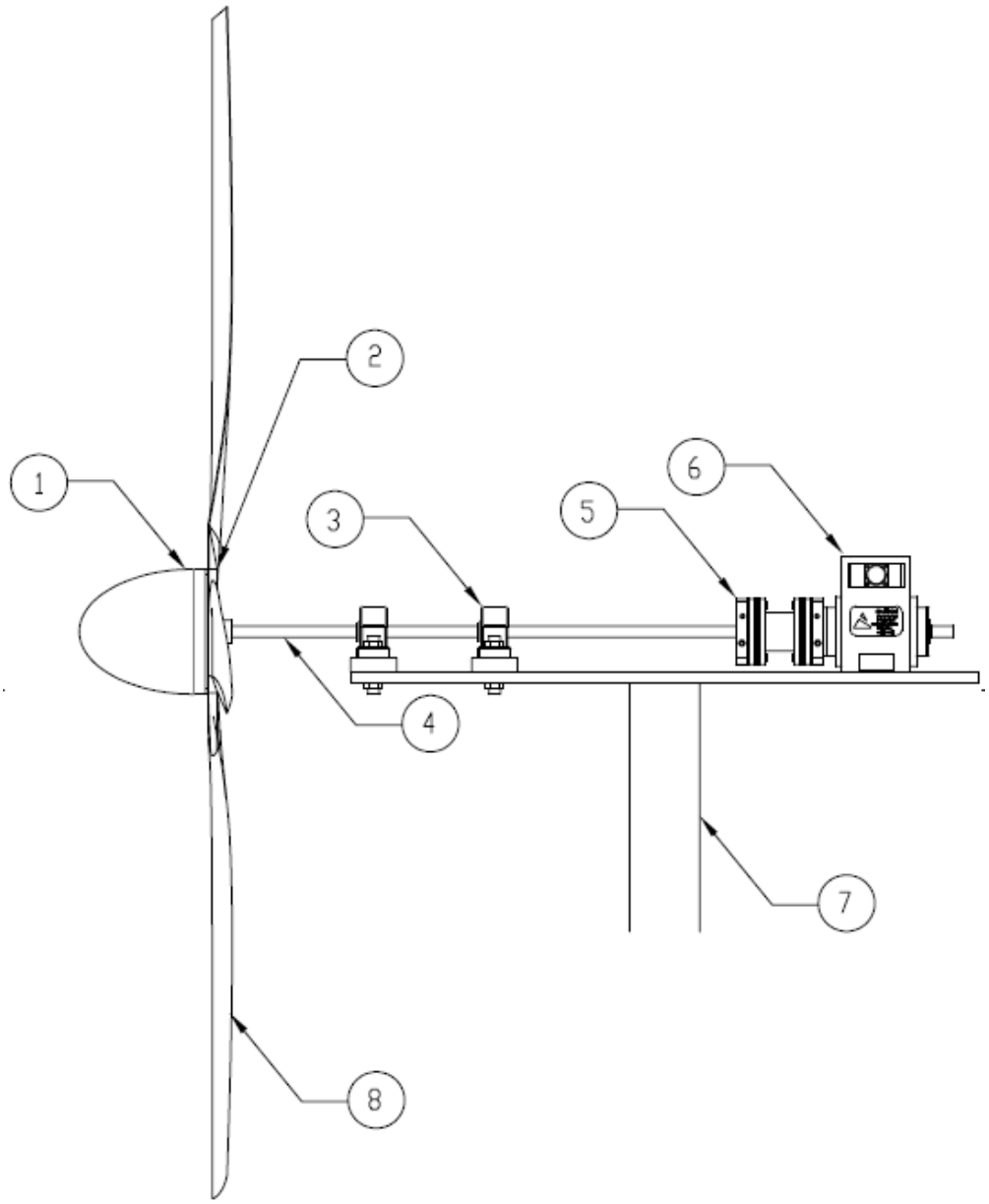


**Figure 63.** Side view of experimental set up.

**Table 7.** Wind turbine components.

| Component | Description |
|---|---|
| 1 | Nose cone |
| 2 | Hub |
| 3 | Bearing housing unit |
| 4 | Shaft |
| 5 | Flexible coupling |
| 6 | Torque Transducer |
| 7 | Stand |
| 8 | Blade |

# APPENDIX B – WIND TURBINE BADE DESIGN CALCULATION

**Table 8.** Optimum blade design calculation.

| Elements | r/R | Selectional Radius (r) mm | Radius of Blade mm (R) | Chord mm | AoA α | c/R | Twist Angle | Angle of Relative Wind |
|---|---|---|---|---|---|---|---|---|
| 1 | 0.16 | 79 | 500 | 70.39 | 5 | 0.36 | 25 | 35.23 |
| 2 | 0.27 | 132 | 500 | 65.19 | 5 | 0.22 | 18.09 | 23.09 |
| 3 | 0.37 | 184 | 500 | 59.98 | 5 | 0.16 | 11.98 | 16.98 |
| 4 | 0.48 | 237 | 500 | 54.78 | 5 | 0.12 | 8.38 | 13.38 |
| 5 | 0.58 | 289 | 500 | 49.57 | 5 | 0.099 | 6.02 | 11.02 |
| 6 | 0.69 | 342 | 500 | 44.36 | 5 | 0.084 | 4.36 | 9.36 |
| 7 | 0.79 | 394 | 500 | 39.16 | 5 | 0.072 | 3.14 | 8.13 |
| 8 | 0.90 | 447 | 500 | 33.95 | 5 | 0.064 | 2.19 | 7.19 |
| 9 | 1 | 500 | 500 | 28.75 | 5 | 0.057 | 1.45 | 6.44 |

# APPENDIX C – CONGRESS PUBLICATION

25th ABCM International Congress of Mechanical Engineering
October 20-25, 2019, Uberlândia, MG, Brazil

## COB-2019-0631
## EXPERIMENTAL MEASUREMENTS ON BIOMIMETIC WIND TURBINE BLADES BY Q. MULTIFLORA SEED

**Lohanna Ferreira Paiva**
**Odenir de Almeida**
Experimental Aerodynamics Research Center (CPAERO), Federal University of Uberlandia, Uberlandia – MG
lohannap@yahoo.com.br; odenir.almeida@ufu.br
**Helena Maura Torezan Silingardi**
Institute of Biology (ICBIO), Federal University of Uberlandia, Uberlandia – MG
torezan.silingardi@ufu.br

***Abstract.*** *Inspired by wind dispersing seeds, this paper presents the performance study of a small-prototype horizontal axis wind turbine (HAWT) by means of low-speed wind tunnel testing. The rotor blade design was based on the Q. Multiflora seed from the Brazilian's Cerrado vegetation. To evaluate and compare the power coefficient, $c_p$, a baseline conventional rotor blade was built entirely based on Blade Element Momentum (BEM) theory. Both small HAWT have been tested for low wind speeds commonly found in countryside of Brazil, such as 4 up to 6 m/s. An experimental workbench was designed and built to properly measure the rotational speed, output power and torque for the prototype tested. The choice of wind dispersing seed, such as Q. Multiflora has shown potential for future insights on designing's inspired by nature.*

***Keywords:*** *biomimetic, wind turbine, Q. Multiflora, blade shape, aerodynamics*

### 1. INTRODUCTION

The global wind potential has motivated projects for the design and optimization of wind turbines for the different application ranges. Brazil, in this scenario, presents a timid participation of the wind power in its energy matrix, however this situation is changing gradually.

Among possible ways of research, we have the interdisciplinarity between engineering and Biomimetics, a science inspired by nature to design innovative solutions, has contributed significantly in this context, especially in the mimesis of seeds and fruits dispersed by anemochories. Its basic principle is to have nature as a model, measure and mentor of the design process (Queiroz et al. 2016). In the field of wind energy this holistic science has fostered significant technological development.

In this context, this research, inspired by a seed that enable robust aerodynamic force production and stable flight, proposes a simplified initial (preliminary) biomimetic blade model (prototype) for horizontal axis wind turbine (HAWT) rotor blade with the objective of evaluating the mimesis potential of the schizocarp of seeds of anemochory species of the Brazilian *Cerrado* and achieving a high integral power coefficient, Cp, over a broad range of tip-speed ratios, and hence enhances robustness in aerodynamic performance. As mentioned, this is an ongoing research started at the end of 2018 and improving along the upcoming years, since it is necessary a broad spectrum of methodologies and interdisciplinarity to correctly evaluate this mimesis effect in the HAWT.

### 2. LITERATURE REVIEW

#### 2.1. Horizontal axis wind turbine (HAWT)

Horizontal axis wind turbines are the most common type of wind turbine used commercially and domestically nowadays. As these turbines are parallel to the direction of the free flow, they are called the horizontal axis wind turbine. The HAWT propulsion principle works with the fundamental principle of lift, as shown in Fig. 1. In this way, the torque generated to rotate the turbine is produced as a result of the pressure difference on the upper and lower surfaces of the wind turbine blade. One of the advantages of using a horizontal axis wind turbine is listed below:

- Highly efficient in terms of energy extraction from the wind;
- Proven reliability as it has been used extensively in the commercial applications;
- Cost effective.

# TORQUE TRANSDUCERS

## TM, TMHS & TMB In-Line Transducers

Magtrol's In-Line Torque Transducers deliver precise torque and speed measurement over a very broad range. Each model has an integrated conditioning electronic module providing 0 to ±10 V DC torque output and an open collector speed output.

## TF Torque Flange Sensors

Based on strain-gauge technology, the TF Sensor's precise telemetry system enables highly accurate signal transmission between its measuring flange, HF transmitter and receiver/conditioner. Special designs available on request.


**TORQUE TRANSDUCER RATINGS**

| Model | | Nominal Rated Torque | | TMB Series *Basic Accuracy* | | TM Series *High Accuracy* | | TMHS Series *High Speed & Accuracy* | | TF Series *Torque Flange Sensor* | |
|---|---|---|---|---|---|---|---|---|---|---|---|
| TM | TF | *N-m* | *lb-ft* | Accuracy Class | Max. Speed *rpm* | Accuracy Class | Max. Speed *rpm* | Accuracy Class | Max. Speed *rpm* | Accuracy Class | Max. Speed* *rpm* |
| 301 | --- | 0.1 | 0.07 | N/A | | 0.2% | 20,000 | N/A | | N/A | |
| 302 | --- | 0.2 | 0.15 | N/A | | < 0.1% | 20,000 | N/A | | N/A | |
| 303 | --- | 0.5 | 0.37 | < 0.1% | 6,000 | < 0.1% | 20,000 | < 0.1% | 40,000 | N/A | |
| 304 | --- | 1 | 0.7 | < 0.1% | 6,000 | < 0.1% | 20,000 | < 0.1% | 50,000 | N/A | |
| 305 | --- | 2 | 1.5 | < 0.1% | 6,000 | < 0.1% | 20,000 | < 0.1% | 50,000 | N/A | |
| 306 | --- | 5 | 3.7 | < 0.1% | 6,000 | < 0.1% | 20,000 | < 0.1% | 50,000 | N/A | |
| 307 | --- | 10 | 7.4 | < 0.1% | 6,000 | < 0.1% | 20,000 | < 0.1% | 50,000 | N/A | |
| 308 | --- | 20 | 15 | < 0.1% | 6,000 | < 0.1% | 20,000 | < 0.1% | 50,000 | N/A | |
| 309 | 309 | 20 | 15 | < 0.1% | 4,000 | < 0.1% | 10,000 | < 0.1% | 32,000 | < 0.1% | 17,000 |
| 310 | 310 | 50 | 37 | < 0.1% | 4,000 | < 0.1% | 10,000 | < 0.1% | 32,000 | < 0.1% | 17,000 |
| 311 | 311 | 100 | 74 | < 0.1% | 4,000 | < 0.1% | 10,000 | < 0.1% | 32,000 | < 0.1% | 17,000 |
| 312 | 312 | 200 | 148 | < 0.1% | 4,000 | < 0.1% | 10,000 | < 0.1% | 24,000 | < 0.1% | 17,000 |
| 313 | 213 | 500 | 369 | < 0.1% | 4,000 | < 0.1% | 10,000 | < 0.1% | 24,000 | < 0.1% | 13,000 |
| 314 | 214 | 1,000 | 738 | N/A | | < 0.1% | 7,000 | < 0.1% | 16,000 | < 0.1% | 13,000 |
| 315 | 215 | 2,000 | 1,475 | N/A | | < 0.1% | 7,000 | < 0.1% | 16,000 | < 0.1% | 10,000 |
| 316 | 216 | 5,000 | 3,688 | N/A | | < 0.1% | 5,000 | < 0.1% | 12,000 | < 0.1% | 8,000 |
| 317 | 217 | 10,000 | 7,375 | N/A | | < 0.15% | 5,000 | < 0.15% | 12,000 | < 0.1% | 8,000 |
| --- | 218 | 20,000 | 14,751 | N/A | | N/A | | N/A | | < 0.25% | 3,000 |
| --- | 219 | 50,000 | 36,878 | N/A | | N/A | | N/A | | < 0.25% | 3,000 |
| --- | 220 | 100,000 | 73,756 | N/A | | N/A | | N/A | | < 0.30% | 3,000 |

** High speed and higher torque versions available on request.*

## Torque Transducer Displays

Magtrol offers two different torque displays: Model 3411 for all TM/TMHS/TMB and TF Transducers and Model 6400 (for TM series only). Both units supply power to the transducer and display torque, speed and mechanical power.

*Model 3411*

## SPECIFICATIONS

| MODEL | | MIC-X-0018 | MIC-X-0039 | MIC-X-0156 | MIC-X-0617 | MIC-X-02470 | MIC-X-3620 |
|---|---|---|---|---|---|---|---|
| **RATINGS** | | | | | | | |
| Rated Torque | [N·m] | 0.18 | 0.39 | 1.56 | 6.17 | 24.7 | 36.2 |
| Maximum Torque | [N·m] | 0.26 | 0.54 | 2.19 | 8.64 | 34.6 | 50.7 |
| Maximum Speed [a] | [rpm] or [$min^{-1}$] | 50000 | 50000 | 50000 | 45000 | 35000 | 30000 |
| Torsional Spring Rate [b] | [N·m/rad] x $10^2$ | 1.586 | 3.89 | 25.986 | 39.768 | 103.5 | 161.76 |
| **MISALIGNMENT** | | | | | | | |
| Axial [b] | [mm] | 0.4 | | | 0.8 | | |
| Radial [c] | [mm] | 0.36 | 0.48 | 0.49 | 0.41 | 0.36 | |
| Angular [b] | [°] | 2 | | 1.5 | 1 | 0.7 | |
| **MOMENT OF INERTIA** | | | | | | | |
| MIC-5-xxxx [d] | [kg·$m^2$] x $10^{-6}$ | - [e] | 2.33 | 14.01 | 37.99 | 104.28 | 203.55 |
| MIC-6-xxxx [d] | [kg·$m^2$] x $10^{-6}$ | - [e] | 1.83 | 11.10 | 28.56 | 78.61 | 159.40 |
| **MECHANICAL CHARACTERISTICS** | | | | | | | |
| Diameter Range [f] | ø[mm]H7 | 2.38 - 7 | 3 - 10 | 4 - 14 | 6 - 18 | 8 - 24 | 7.5 - 28 |
| Balancing Quality | | G2.5 according to ISO1940 | | | | | |
| Weight max. | [g] | - [e] | 28 | 77 | 133 | 260 | 355 |

a) The specified maximum speed may require specific balancing. By default, Magtrol delivers couplings without balancing.

b) Axial and angular misalignments and torsional spring rate refer to single-element coupling (MIC-6-xxxx).

c) Radial misalignments refer to double element coupling (MIC-5-xxxx).

d) At maximum bore

e) Value available on request.

f) The standard versions are manufactured with integer values; the standard tolerance is H7. All diameters and tolerances are possible. Please contact our sales department.

# ANNEX B – SCANNER


**Figure 64.** 3D STRUCTURED LIGHT SCANNER RANGE VISION STANDARD PLUS.

**Figure 65.** SCAN STRATEGY: Automatic rotating base.

**Table 9.** Scanner specifications.

| Scanning area number | [ 1 ] | [ 2 ] | [ 3 ] | [ 4 ] | [ D700 ] |
|---|---|---|---|---|---|
| Scanning Area (WxHxD) (mm) | 460*345*345 | 300*225*225 | 133*100*100 | 66*50*50 | 920*690*690 |
| 3D point accuracy* | 0.085 mm | 0.05 mm | 0.03 mm | 0.03 mm | 0.16 mm |
| 3D resolution: | | | | | |
| Standard/ Standard Plus | 0.35 mm | 0.23 mm | 0.1 mm | 0.05 mm | 0.7 mm |
| Advanced | 0.3 mm | 0.2 mm | 0.085 mm | 0.043 mm | 0.6 mm |
| Premium | 0.18 mm | 0.12 mm | 0.05 mm | - | 0.35 mm |
| Operating distance | 0.9 m | 0.52 m | 0.3 m | 0.27 m | 2 m |

| Model | Standard | Standard Plus | Advanced | Premium |
|---|---|---|---|---|
| Resolution of cameras | 1,3 Mpix | 1,3 Mpix | 2 Mpix | 5 Mpix |
| Matrix diagonal, body of the cameras | 1/2”, plastic | 1/1.8”, metal | 1/1.8”, metal | 2/3”, metal |
| Scanning time | ~ 7 sec | ~ 7 sec | ~ 12 sec | ~ 15 sec |
| Model calculation time | ~ 5 sec | ~ 5 sec | ~ 10 sec | ~ 20 sec |
| Scanning black | - | - | + | + |